This article has been accepted for publication in IEEE Open Journal of Power Electronics. This is the author's version which has not been fully edited and content may change prior to final publication. Citation information: DOI 10.1109/OJPEL.2026.3734120

Received 22 August, 2025; revised XX Month, XXXX; accepted XX Month, XXXX; Date of publication XX Month, XXXX; date of current version XX Month, XXXX.

Digital Object Identifier 10.1109/OJPEL.2025.xxxxxxx

Impact of Control Architecture on Grid-Forming Inverters Under Grid Disturbances

Jan Wachter[1], ***Student Member, IEEE,*** **Gab-Su Seo**[2], ***Senior Member, IEEE,*** **Lutz Gröll**[1] **and Veit Hagenmeyer**[1], ***Member, IEEE***

[1]Institute for Automation and applied Informatics of the Karlsruhe Institute of Technology (KIT), 76131 Karlsruhe, Germany
[2]Power Systems Engineering Center, National Laboratory of the Rockies (NLR), Golden, CO 80401, USA

CORRESPONDING AUTHOR: Jan Wachter (e-mail: jan.wachter@kit.edu).

This work was authored in part by the National Laboratory of the Rockies for the U.S. Department of Energy (DOE) under Contract No. DE-AC36-08GO28308. Funding for the National Laboratory of the Rockies author only provided by the U.S. Department of Energy Office of Energy Efficiency and Renewable Energy Solar Energy Technologies Office Agreement Number 38637.

ABSTRACT In inverter-dominant power systems where grid-forming inverters maintain system voltage and frequency, understanding the impact of fast-timescale responses of inverter-based resources to grid disturbances is critical. This paper investigates how the cascaded control architecture and implementation of grid-forming inverter controls impact their response to such disturbances. Focusing on fast-timescale behavior, the study evaluates the influence of inner control loops, comparing virtual admittance and proportional-integral/resonant voltage control, as well as the selected control reference frame (i.e., rotating or stationary). To examine the role of primary control on transient performance, we consider droop-based and virtual synchronous machine-based grid-forming control. Through detailed simulation studies and hardware experiments of grid-forming inverters under grid disturbances, including voltage sags, phase-angle jumps, and rapid frequency changes, this paper examines how control architecture choices shape the fast-timescale response of grid-forming inverters during transients. The results show that voltage control architecture and reference frame significantly affect transient response. For the considered setups and used tuning procedures, virtual-admittance yields larger maximum currents than proportional-integral/resonant voltage control, and rotating-frame proportional-integral voltage control shows improved damping compared to the stationary-frame alternative.

INDEX TERMS Grid-forming inverter, control architecture, reference frame, grid support, transient performance.

I. Introduction

One of the prominent developments in modern power grids is the increasing penetration of power-electronic-interfaced devices [1]. This unprecedented trend has several significant consequences [2], [3], among others: (i) decreased physical inertia causing faster grid dynamics, which increases the importance of the fast-timescale response of grid-connected devices; (ii) the behavior of power-electronic devices is determined by their control system, highlighting the critical role of the control system design.

In the timescale of seconds, which is slow relative to inverter-based resources (IBRs), the power output can be flexibly adjusted within IBRs' safe operating range. This makes such devices well dispatchable on slow timescales, enabling the implementation of various grid-support functions provided by both grid-following (GFL) and grid-forming (GFM) IBRs. Such services are based on adapting the power exchanged with the grid in response to *measured* changes in frequency and voltage amplitude. These grid-supportive capabilities of distributed IBRs are beneficial for the power grid [4] and can offer an economically feasible alternative to conventional system inertia [5]. The significance of these services is evident by their inclusion in grid codes for distributed devices [6], [7], and the development of control energy markets that support their deployment in various global power systems [4], [8]. Notably, such

This work is licensed under a Creative Commons Attribution 4.0 License. For more information, see https://creativecommons.org/licenses/by/4.0/

This article has been accepted for publication in IEEE Open Journal of Power Electronics. This is the author's version which has not been fully edited and content may change prior to final publication. Citation information: DOI 10.1109/OJPEL.2026.3734120

services must be provided more rapidly than conventional primary control reserve, due to the faster dynamics of IBR-driven power systems. As IBR penetration rises further, faster grid services traditionally provided by synchronous machine inertia must increasingly be delivered by IBRs. This initial, small-timescale response between a grid event and the full deployment of other grid services is critical for riding through disturbances, as unexpected device trips or behavior can lead to cascading outages [2]. Therefore, it is essential to analyze the *initial* response of IBRs during transient grid disturbances.

Previous studies have focused on the role of primary control schemes in enabling grid services, including their application in microgrids [9]–[14]. While these studies examine the influence of the primary control, the impact of inner control loops, such as voltage and current control, is often overlooked due to the focus on slower timescales. A comparison of two inner control loop architectures under varying load conditions is presented in [15], highlighting their impact on system performance. In [16], different inner-loop control architectures are compared by considering the frequency-dependent input admittance of the respective systems. Narula et al. [16] compare inner control structures in terms of harmonic damping, stability, and performance under varying grid strength. In [17], the advantage of a sliding mode control-based finite control set model predictive control for voltage control of GFM inverters is discussed. Beza et al. in [18] examine how control strategies influence resonance interactions between IBRs and the power grid. In conclusion, these studies compare inner-loop architectures for harmonic damping, resonance interaction, or steady-state performance; however, their influence on fast-timescale transient response to grid disturbances remains insufficiently studied.

The main contribution of this paper is the systematic comparison of how established control architectures, inner control loops, and controller tuning influence the behavior of grid-forming (GFM) inverter-based resources during grid disturbances, and the demonstration that these choices significantly influence the fast-timescale behavior. Based on the obtained simulation and experiment results, design-oriented insights are derived. For this, this paper:

- systematically quantifies how key design choices, including virtual admittance control versus proportional-integral (PI) or proportional-resonant (PR) voltage control, stationary versus rotating reference frames, primary control scheme, current control loop tuning, and common design assumptions, affect the disturbance response of GFM IBRs. As grid disturbances, we consider three scenarios: voltage sag, phase angle jump, and a rate of change of frequency (ROCOF) event. All events are designed not to trigger current limitation, to allow for focusing on the controller-induced behavior without current limiting that can significantly shape the inverter dynamics, preventing gaining insights into the normal operation [19]. The results are obtained from a consistent design and comparison framework that combines reproducible simulations and hardware experiments to include relevant real-world effects.
- shows that inner control loops, in particular the choice of voltage control architecture and reference frame, have a significant impact on the fast timescale behavior with respect to voltage support, current overshoot, and settling time. Furthermore, tuning the current control, especially for the stationary reference frame implementation, provides additional degrees of freedom to shape the disturbance response. The qualitative results are observed over a broad parameter range in both simulation and hardware experiments.
- analyzes and discusses the underlying mechanisms contributing to the observed behavior from a disturbance perspective. Based on the results, we derive design-oriented insights to guide practical applications.

The remainder of this paper is structured as follows. Section II describes the design framework, including the system under study and the considered GFM inverter control architectures in detail. Next, Section III introduces the grid disturbance scenarios, performance metrics, and test setups, followed by an analysis of simulation and hardware experiment results. Subsequently, in Section IV, the results are summarized and discussed from a design perspective. Finally, Section V concludes the paper and offers an outlook on future research directions.

II. System Under Study

Fig. 1 presents the single inverter infinite-bus system on which the control system design framework is based. The two considered test setups are discussed in Section III.B and the component values are summarized in Table 1. To reflect typical phenomena observed in practical systems, the pu values for the two test setups are in typical ranges for grid-connected inverters.

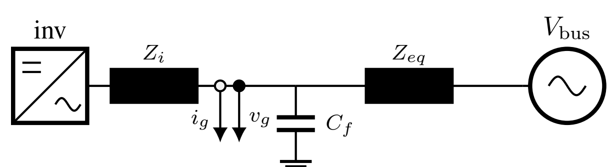

FIGURE 1. **Considered setup for the study: inverter (inv), impedance of the grid connection inductor $Z_i = R_i + jX_i$, filter capacitor C_f and the equivalent impedance $Z_{eq} = R_{eq} + jX_{eq}$ which entails the line impedance as well as other relevant impedance, e.g. grid-side inductor of LCL-filter, and the infinite bus voltage source (V_{bus}). Further, it illustrates the voltages and currents used to calculate the derived values.**

A. Details of the Compared Control Approaches

Fig. 2 shows an overview of the control approaches that are compared and the abbreviations used throughout the remainder of the paper. Fig. 3 and Fig. 4 depict the virtual admittance (VA) and PI/PR-based voltage control architectures considered in this work, respectively. Throughout the paper,

TABLE 1. Test system parameters. $X_x = \omega_0 L_x$, where L_x is the considered inductance and ω_0 is the respective grid base frequency.

Sym.	Setup-A	Setup-B	Description
R_i	$2.5 \cdot 10^{-2}$ pu	$9.4 \cdot 10^{-3}$ pu	inverter-side resistance
X_i	$5.7 \cdot 10^{-3}$ pu	$5.2 \cdot 10^{-2}$ pu	inverter-side impedance
C_f	$3.02 \cdot 10^{-2}$ pu	$2.4 \cdot 10^{-2}$ pu	filter capacitance
R_{eq}	$4.9 \cdot 10^{-3}$ pu	$13.7 \cdot 10^{-3}$ pu	equivalent resistance
X_{eq}	$7.7 \cdot 10^{-2}$ pu	$1.01 \cdot 10^{-1}$ pu	equivalent impedance

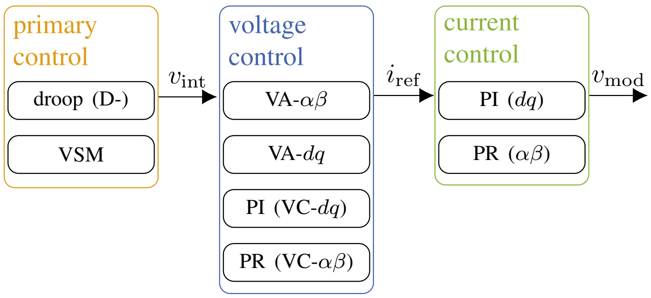

FIGURE 2. Control architectures studied. The abbreviations VSM (virtual synchronous machine) and VA (virtual admittance) are used.

superscripts dq, $\alpha\beta$, and abc denote the reference frame. In some cases, it is omitted where not necessary or needed for generality.

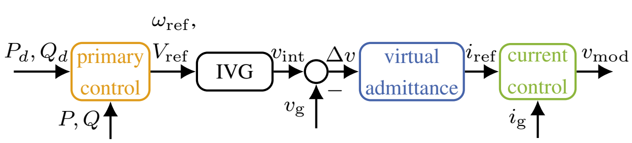

FIGURE 3. Cascaded control scheme for virtual admittance control. Depending on the considered dq or $\alpha\beta$ reference frame, the internal voltage generation (IVG), virtual admittance, and current control are realized accordingly.

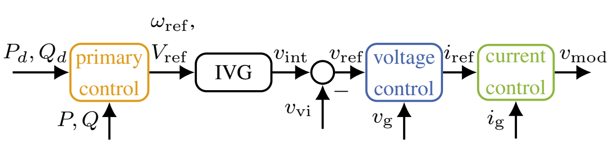

FIGURE 4. Cascaded control scheme for PI/PR-based voltage control. Depending on the considered dq or $\alpha\beta$ reference frame, the internal voltage generation (IVG), voltage control, and current control are realized accordingly.

1) Internal voltage generator (IVG)

This subsystem generates the internal voltage from the given voltage amplitude $V_{\text{ref}}(t)$ and angular frequency $\omega_{\text{ref}}(t)$ provided by the primary control. To obtain the internal angle $\theta(t)$, the reference angular frequency $\omega_{\text{ref}}(t)$ is integrated s.t. $\frac{\mathrm{d}}{\mathrm{d}t}\theta(t) = \omega_{\text{ref}}(t), \quad \theta(0) = \theta_0, \quad \theta(t) \in \mathbb{R}/2\pi\mathbb{Z}$ with equivalence classes on $[0, 2\pi)$. The resulting internal voltage is given by

$$v_{\text{int}}^{\alpha\beta} = \begin{bmatrix} V_{\text{ref}}(t)\cos(\theta(t)) \\ V_{\text{ref}}(t)\sin(\theta(t)) \end{bmatrix}, \quad v_{\text{int}}^{dq} = \begin{bmatrix} V_{\text{ref}}(t) \\ 0 \end{bmatrix}. \tag{1}$$

2) Virtual admittance-based control

Virtual admittance-based control is an alternative to traditional voltage control loop architecture, see [20], [21], to obtain a reference current based on the voltage difference between the internal voltage vector and the measured grid voltage (see Fig. 3). It can be expressed as $\hat{i}_{\text{ref}}(s) = T_{va}\,\Delta\hat{v}(s)$, the superscript $\hat{}$ denotes Laplace transformed signals and T_{va} depends on the reference frame as following [22]:

$$T_{va}^{\alpha\beta} = \begin{bmatrix} sL_{\text{v}} + R_{\text{v}} & 0 \\ 0 & sL_{\text{v}} + R_{\text{v}} \end{bmatrix}^{-1}, \tag{2}$$

$$T_{va}^{dq} = \begin{bmatrix} sL_{\text{v}} + R_{\text{v}} & -\omega_0 L\text{v} \\ \omega_0 L_{\text{v}} & sL_{\text{v}} + R_{\text{v}} \end{bmatrix}^{-1}, \tag{3}$$

where the tunable parameters are the virtual inductance L_{v} and the virtual resistance R_{v}, and ω_0 is the nominal angular frequency.

3) Virtual impedance for PI/PR-based voltage control

We implement a virtual impedance for the PI/PR-based voltage control approach to achieve steady-state equivalence with the virtual admittance approach. Here, not the reference current inferred from the difference between the internal and grid voltages is calculated, but the voltage drop across the virtual impedance caused by the grid current. This virtual impedance modifies the internal voltage vector according to the injected current, $v_{\text{ref}} = v_{\text{int}} - v_{\text{vi}}(i_g)$. To avoid numerical differentiation of measured signals, the well-established approximation [23] is used to obtain v_{vi}:

$$v_{\text{vi}} = \begin{bmatrix} R_v & -\omega_0 L_v \\ \omega_0 L_v & R_v \end{bmatrix} i_g\,, \tag{4}$$

where v_{vi}, i_g can be in either dq or $\alpha\beta$-frame. Note that due to the approximation of the current derivative, the above equation is only exact for the steady state and nominal frequency.

B. Current Control Design

The current controller can be realized in $\alpha\beta$ or dq-frame. The highly simplified model depicted in Fig. 5 is widely used for the current controller design in both reference frames [24], [25].

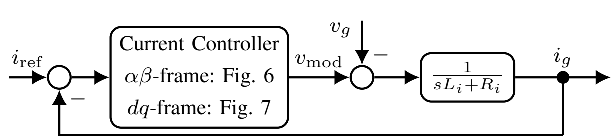

FIGURE 5. Control model for the design of the current controller.

1) Stationary reference frame current control design

A typical PR controller transfer function is given by [25], [26]:

$$G_{cc}^{\alpha\beta}(s) = k_p^{\alpha\beta} + k_r^{\alpha\beta}\,\frac{2\omega_c s}{s^2 + 2\omega_c s + \omega_0^2}\,, \tag{5}$$

where $k_p^{\alpha\beta}$, $k_r^{\alpha\beta}$ are controller parameters, ω_c is the tunable width of the resonant peak [25]. The open-loop transfer function is given by:

$$H_{ol,cc}^{\alpha\beta}(s) = \left(k_p^{\alpha\beta} + k_r^{\alpha\beta}\,\frac{2\omega_c s}{s^2 + 2\omega_c s + \omega_0^2}\right)\frac{1}{sL_i + R_i}\,. \tag{6}$$

By choosing a desired gain crossover frequency $\omega_{\mathrm{gc,cc}} \gg \omega_0$, the resonant term has negligible influence at the crossover frequency [25], [26]. We choose $\omega_{\mathrm{gc,cc}} = 20\,\omega_0$. This is a reasonable value that guarantees sufficient distance from the switching frequency [24] as well as the nominal frequency. At the gain crossover frequency by definition $|H_{ol,cc}^{\alpha\beta}(j\omega_{\mathrm{gc,cc}})| = 1$ holds. Using this relation, we obtain:

$$k_p^{\alpha\beta} = \sqrt{R_i^2 + (\omega_{\mathrm{gc,cc}}\,L_i)^2}\,. \tag{7}$$

Inserting (7) in (6) at the resonant frequency $s = j\omega_0$ yields:

$$k_r^{\alpha\beta} = p_{g,cc}\sqrt{(\omega_0 L_i)^2 + R_i^2} - \sqrt{(\omega_{\mathrm{gc,cc}} L_i)^2 + R_i^2}\,, \tag{8}$$

where $p_{g,cc} = |H_{ol,cc}^{\alpha\beta}(j\omega_0)|$ is the desired resonance peak gain, which is used as a tuning parameter. The structure, including the internal voltage feedforward, is shown in Fig. 6, where v_{mod}^{abc} denotes the modulation voltage in natural coordinates.

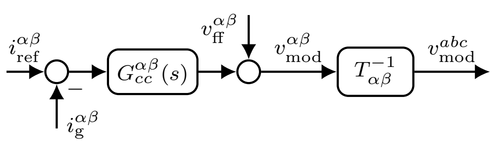

FIGURE 6. Current controller in stationary reference frame. The inverse Clarke transformation is given by $T_{\alpha\beta}^{-1}$, $i_g^{\alpha\beta}$ denotes the measured grid current and $v_{\mathrm{ff}}^{\alpha\beta}$ the feedforward voltage.

2) Synchronous reference frame current control design

The following considerations are inspired by [24], [27]. The deployed PI controller is given by:

$$G_{cc}^{dq}(s) = k_{p,cc}^{dq} + \frac{k_{i,cc}^{dq}}{s}\,. \tag{9}$$

This choice yields the following open-loop transfer function:

$$H_{ol,cc}^{dq}(s) = \frac{k_{p,cc}^{dq}\,s + k_{i,cc}^{dq}}{L_i\,s^2 + R_i\,s}\,. \tag{10}$$

We cancel the stable pole $s = -\frac{R_i}{L_i}$ with the zero of the PI controller by selecting the gains as:

$$\frac{k_{i,cc}^{dq}}{k_{p,cc}^{dq}} = \frac{R_i}{L_i}\,. \tag{11}$$

This yields the following first-order closed-loop response:

$$G_{cl,cc}(s) = \frac{H_{ol,cc}^{dq}(s)}{1 + H_{ol,cc}^{dq}(s)} = \frac{\omega_{\mathrm{gc,cc}}}{s + \omega_{\mathrm{gc,cc}}}\,, \tag{12}$$

where $\omega_{\mathrm{gc,cc}} = \frac{k_{p,cc}^{dq}}{L_i}$. Therefore, we can prescribe the desired closed-loop bandwidth of the system by the appropriate choice of $k_{p,cc}^{dq}$. This yields the following choice of the PI controller parameters $k_{p,cc}^{dq} = \omega_{\mathrm{gc,cc}}\,L_i$, $k_{i,cc}^{dq} = \omega_{\mathrm{gc,cc}}\,R_i$. The resulting scheme, including the internal voltage feed-forward and decoupling network, is depicted in Fig. 7. The cross-coupling matrix is given by:

$$T_{cc} = \begin{bmatrix} 0 & -1 \\ 1 & 0 \end{bmatrix}\omega_0 L_i\,, \tag{13}$$

which is required since the design approach assumes decoupled dq axes [28], [29].

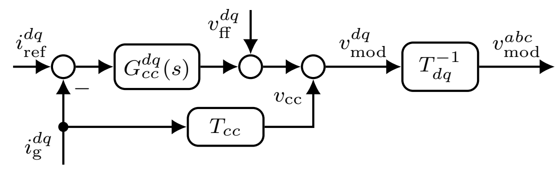

FIGURE 7. Current controller in synchronous reference frame. The inverse Park transformation is given by T_{dq}^{-1}, i_g^{dq} denotes the measured grid current and v_{ff}^{dq} the feedforward voltage.

3) Comparison of the tuning results for the current control

To assess the comparability of the two current control implementations, we compare their open-loop Bode plots. The parameters for both approaches are chosen to achieve the same closed-loop system bandwidth, a common practice [24], [25]. Note that in order to enable reliable operation under non-ideal grid conditions, e.g., at frequencies deviating from ω_0, the resonance peak of the PR control must be altered using the resonant peak width coefficients, ω_c and peak gain $p_{g,cc}$. For PI control in dq-frame, the resonant peak tracks the inverter's internal reference frame frequency. For steady-state operation, this aligns with the grid frequency via the synchronization property of primary control. However, during transients, the internal frequency may differ from the grid frequency.

Further, note that the aim is not to tune the controllers identically, but to evaluate performance using tuning that achieves the same design goal: matching the closed-loop bandwidth in this study. Fig. 8 compares the open-loop Bode plots, which show good agreement in the relevant frequency range around the nominal frequency. Note that the dq-frame controller was translated to the rotating reference frame as shown in [26].

C. Voltage Control Design

Again, the voltage controller can be realized in $\alpha\beta$ or dq-frame. The dynamics of the closed-loop current control are

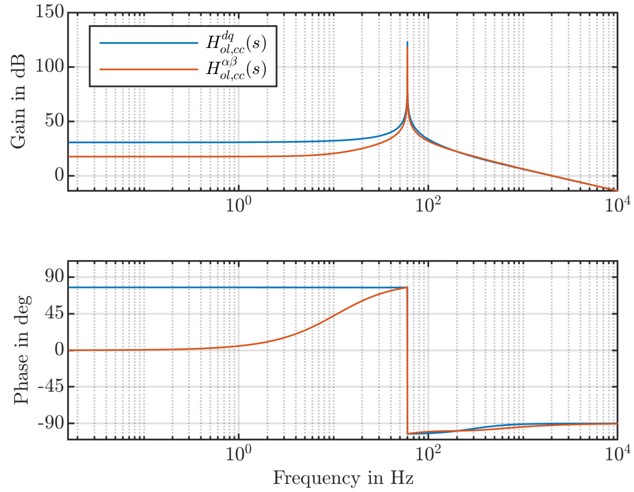

FIGURE 8. **Comparison the Bode plots of the current controller in $\alpha\beta$ coordinates (5) and dq coordinates (9) in the stationary reference frame for Setup-A.**

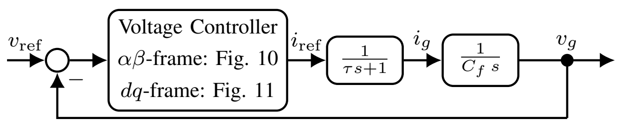

FIGURE 9. **Control model for the design of the voltage controller.**

modeled as a first-order system [24], [25], characterized by the time constant $\tau = \frac{1}{\omega_{gc,cc}}$. Fig. 9 shows this widely adopted control model. For both synchronous and stationary reference frames, the same structure is used, which again implies the assumption of decoupled axes.

1) Stationary reference frame voltage control design

Again, a PR controller is chosen for the voltage controller

$$G_{vc}^{\alpha\beta}(s) = k_{p,vc}^{\alpha\beta} + k_{r,vc}^{\alpha\beta} \frac{2\omega_{c,vc}s}{s^2 + 2\omega_{c,vc}s + \omega_0^2}\,, \tag{14}$$

where $k_{p,vc}^{\alpha\beta}$, $k_{r,vc}^{\alpha\beta}$ are controller parameters, and $\omega_{c,vc}$ defines the width of the resonant peak [25]. The open-loop transfer function can be expressed as

$$H_{ol,vc}^{\alpha\beta}(s) = G_{vc}^{\alpha\beta}(s)\frac{1}{(\tau s+1)C_f s}\,. \tag{15}$$

Again, we choose a desired gain crossover frequency that is larger than the resonance frequency $\omega_{\mathrm{gc,vc}} \gg \omega_0$, which justifies neglecting the resonant part of the controller for the following consideration. To ensure the necessary timescale separation between the current and voltage control loop, we choose $\omega_{\mathrm{gc,vc}} = 0.1\,\omega_{\mathrm{gc,cc}}$, which is within typically used values e.g. [25]. Using the definition of the gain crossover frequency $|H_{ol,\mathrm{vc}}^{\alpha\beta}(j\omega_{\mathrm{gc,vc}})| = 1$ we obtain:

$$k_{p,vc}^{\alpha\beta} = C_f \omega_{\mathrm{gc,vc}} \sqrt{(\tau\omega_{\mathrm{gc,vc}})^2 + 1}\,. \tag{16}$$

Using the resonant gain $p_{g,vc} = |H_{ol,vc}^{\alpha\beta}(j\omega_0)|$ as a tuning parameter yields:

$$k_{r,vc}^{\alpha\beta} = p_{g,vc} C_f \omega_0 \sqrt{(\tau\omega_0)^2 + 1} - k_{p,vc}^{\alpha\beta}\,. \tag{17}$$

The resulting control scheme is depicted in Fig. 10.

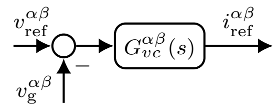

FIGURE 10. **Voltage controller in the stationary reference frame.**

2) Synchronous reference frame voltage control design

In the synchronous reference frame, the controller is chosen as a PI controller:

$$G_{vc}^{dq}(s) = k_{p,vc}^{dq} + \frac{k_{i,vc}^{dq}}{s}\,, \tag{18}$$

where $k_{p,vc}^{dq}, k_{i,vc}^{dq}$ are the controller parameters. For the process:

$$P(s) = \frac{1}{C_f s(\tau s + 1)} \tag{19}$$

we use the symmetrical optimum control approach [30] which is a common approach for this task [24]. This yields the following controller parameters:

$$k_{p,vc}^{dq} = \frac{C_f}{2\,\tau}\,, \quad k_{i,vc}^{dq} = \frac{C_f}{8\,\tau^2}\,. \tag{20}$$

The resulting control scheme, including the cross-coupling, is depicted in Fig. 11. For this, the cross-coupling is given by:

$$T_{vc} = \begin{bmatrix} 0 & -1 \\ 1 & 0 \end{bmatrix} \omega_0\, C_f\,. \tag{21}$$

Again, the cross-coupling is used since the design assumes decoupled dq axes.

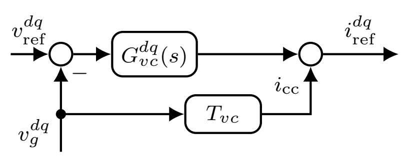

FIGURE 11. **Voltage controller in synchronous reference frame.**

3) Comparison of the tuning results for the voltage control

To evaluate the comparability of the two voltage-control designs, we consider their open-loop frequency responses. For this, the tuning parameters $\omega_{c,vc}$ and $p_{g,vc}$ of the rotating reference frame PR controller are chosen to closely match the bandwidth and resonant gain of the synchronous reference frame controller. As in the current controller design, to enable reliable operation at off-nominal frequencies, the controller resonance peak must be shaped using the resonant peak width $\omega_{c,vc}$ and peak gain $p_{g,vc}$ for PR controllers. For PI control in dq-frame, the resonant peak tracks the inverter's internal reference frame frequency. For steady-state operation, this aligns with the grid frequency via the synchronization property of primary control. However, during transients, the internal frequency may differ from the grid frequency. Fig. 12 compares the open-loop Bode plots, which show good agreement in the relevant frequency range around the nominal grid frequency. Note that the dq-frame controller was translated to the rotating reference frame as shown in [26].

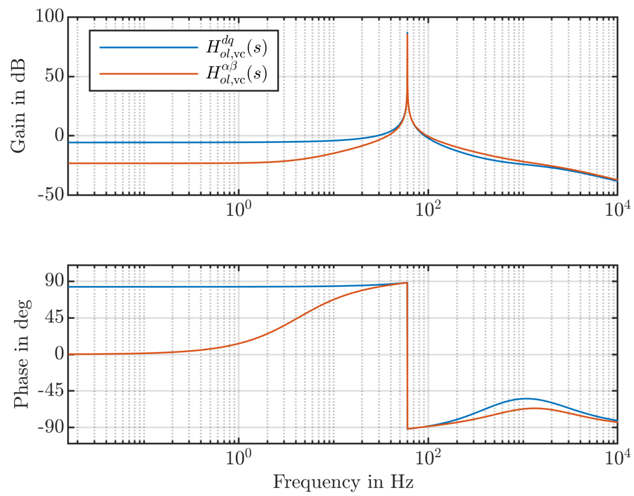

FIGURE 12. **Bode plots of the voltage controller in $\alpha\beta$ (14) and dq (18) in the stationary reference frame for Setup-A.**

D. Primary Control Design

Primary control schemes of GFM inverters generate an internal reference voltage, which is essential for achieving and maintaining synchronism with the grid and enabling the parallel operation of multiple generation systems.

1) Droop-based primary control

A widely adopted primary control scheme is droop control [28]. For inductive grids, the following droop relations are used:

$$\omega_{\mathrm{ref}}(t) = \omega_0 + \frac{k_{Pf}}{2\pi}\left(P_d - P(t)\right), \tag{22}$$

$$V_{\mathrm{ref}}(t) = V_0 + k_{QV}\left(Q_d - Q(t)\right), \tag{23}$$

where $\omega_{\mathrm{ref}}(t)$ and $V_{\mathrm{ref}}(t)$ are the resulting angular frequency and voltage amplitude of the internal voltage, k_{Pf} and k_{QV} are the tunable droop constants, V_0 the nominal voltage amplitude, P_d and Q_d active and reactive power set points, and $P(t)$ and $Q(t)$ the measured powers, respectively. For this study, $P(t)$ and $Q(t)$ are obtained by filtering the instantaneous values with a first-order low-pass filter with a cut-off angular frequency of $\omega_{\mathrm{mc}} = 12\pi\ \mathrm{rad/s}$. The values for k_{Pf} and k_{QV} are chosen such that $5\,\%$ droops with respect to the base values are achieved.

2) VSM-based primary control

The virtual synchronous machine (VSM) design in this work is based on the synchronous power controller [31] concept. A swing equation-based primary controller is chosen, allowing independent tuning of damping, inertia, and steady-state power-frequency droop [32]. Fig. 13 shows the block diagram, where the inner control loops are assumed to have ideal transfer behavior. Note that this VSM design is chosen for independent tuning of steady-state power-frequency droop, allowing the two primary control approaches to be tuned equally with respect to their steady-state behavior. The voltage control loop is identical to that of the droop control (see (23)). For this, we consider a lead-lag type controller

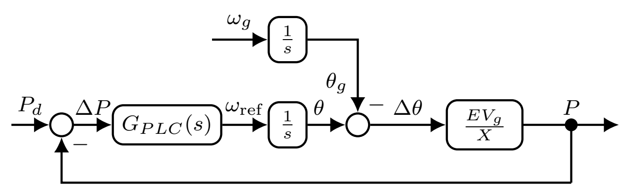

FIGURE 13. **Block diagram of the power synchronization loop including the primary control $G_{PLC}(s)$.**

for the power synchronization loop $G_{PLC}(s)$ [32], [33]

$$G_{PLC}(s) = \frac{k_p\, s + k_i}{s + k_g}\,, \tag{24}$$

where k_p, k_i and k_g the controller parameters. This yields the closed-loop transfer function:

$$\frac{\hat{P}(s)}{\hat{P}_d(s)} = \frac{\frac{EV_g}{X}(k_p\, s + k_i)}{s^2 + s(k_g + \frac{EV_g}{X}k_p) + \frac{EV_g}{X}k_i}\,, \tag{25}$$

where E , V_g are the voltage amplitudes at the inverter output and the point of common coupling, both are assumed to be $1\,\mathrm{pu}$. The dominant impedance of the grid connection is denoted by X, which combines physical and virtual impedance/admittance. To ensure comparability of the tuning with other VSM-based approaches [10], [12] in terms of inertia and damping, the following relations for k_i, k_p, k_g are derived in [33]:

$$k_i = \frac{\omega_0}{2HS_n}\,, \tag{26}$$

$$k_p = \xi\sqrt{\frac{\omega_0 X}{EV_g HS_n}} + \frac{X}{2HEV_g\gamma_d}\,, \tag{27}$$

$$k_g = -\frac{1}{2H\gamma_d}\,, \tag{28}$$

where $\xi = \sqrt{2}$ is the damping and $H = 0.5\,\mathrm{s}$ the inertia constant, and S_n represents the nominal apparent output power of the inverter. Further, γ_d is the desired normalized steady state active power frequency droop, which is defined as:

$$\gamma_d = \frac{\frac{\Delta\omega}{\omega_0}}{\frac{\Delta P}{S_n}} = \frac{S_n}{\omega_0 \underbrace{\frac{\Delta P}{\Delta\omega}}_{=:k_d}} \,, \tag{29}$$

k_d can be obtained from the disturbance sensitivity transfer function:

$$\frac{\hat{P}(s)}{\hat{\omega}_g(s)} = -\frac{\frac{EV_g}{X}(s+k_g)}{s^2 + s(k_g + \frac{EV_g}{X}k_p) + \frac{EV_g}{X}k_i} \,, \tag{30}$$

from which we obtain $k_d = \frac{\hat{P}(0)}{\hat{\omega}_g(0)} = -\frac{k_g}{k_i}$. The parameters are chosen to yield the same steady-state frequency droop of $5\,\%$ as the droop-based primary control.

III. Simulation and Experiment Results

This section first introduces the grid contingency scenarios, performance metrics, and considered test setups in detail. Then, the simulation and experiment results for the considered GFM control approaches in response to the disturbance scenarios are presented and analyzed.

A. Grid Contingency Scenarios and Performance Metrics

1) Considered grid contingency scenarios

These test scenarios are chosen to represent serious grid incidents. Furthermore, they are designed not to activate current limitation, which is considered out of scope for this study, as it may profoundly alter system behavior (interested readers are referred to [34]). The following grid contingencies are considered:

- E1) *Voltage sag:* We consider a voltage sag from $1\,\mathrm{pu}$ to $0.8\,\mathrm{pu}$ as this would be within the range in which devices need to be able to operate indefinitely, yet it is a severe voltage sag for grid-connected inverters to support the grid under off-nominal operating conditions [6], [35]. The voltage amplitude remains at $0.8\,\mathrm{pu}$ after the incident.
- E2) *Phase angle jump:* We consider a $-10\,\mathrm{deg}$ phase angle jump. For GFM IBRs, it is expected to maintain its voltage-source characteristics, naturally yielding active power injection, as suggested by emerging GFM inverter standards [7].
- E3) *Frequency ramp:* In IBR-driven grids, the lack of physical inertia may lead to larger ROCOF [36], therefore we refer $-3\,\frac{\mathrm{Hz}}{\mathrm{s}}$ for $0.5\,\mathrm{s}$ which is taken from the Hawaii microgrid specification [37]. The frequency remains at the final value that it reached after $0.5\,\mathrm{s}$.

2) Initial operating conditions and experiment procedure

For both setups, the initial power setpoints are $P_d = 0.2\,S_{\mathrm{base}}$ and $Q_d = 0$. The grid-phase angle at which the incidents occur are fixed for each setup.

For Setup-A, this is guaranteed by the time-schedule of the simulation: at $t = 0$ the system is initialized, at $t = 0.02\,\mathrm{s}$ the GFM is enabled. After all transients are settled and steady-state operation is reached, the events (E1-E3) are scheduled at $t = 1\,\mathrm{s}$. The initial power angle can be estimated as $\delta_0 = \arcsin(\frac{P_0 X_{eq}}{EV}) \approx 0.8824\,\mathrm{deg}$, assuming both the grid voltage and capacitor voltage are $1\,\mathrm{pu}$. The modulation margin for nominal operation at $1\,\mathrm{pu}$ voltage can be approximated based on the DC-link voltage as $M = 1 - \frac{2\sqrt{2}}{\sqrt{3}}\frac{V_{ref,pu}V_{\mathrm{base}}}{V_{dc}}$ which yields $M = 0.46$ for $V_{\mathrm{dc}} = 3\,\mathrm{pu}$. As no current limitation is implemented for simulation, no meaningful margin can be given. For Setup-A E1, the voltage sag is numerically smoothed as a ramp with a duration of $2\,\mathrm{ms}$.

The experiment procedure for Setup-B is analogous. After the bus is powered, the GFM is connected. After a waiting period of approx $10\,\mathrm{s}$ due to manual steps necessary, all transients are settled, and the incident is triggered. To ensure the same conditions for each experiment run, the incidents are always triggered at the same infinite bus voltage angle $\theta_{\mathrm{trig}} = \pi$. The initial power angle is given by $\delta_0 = \arcsin(\frac{P_0 X_{eq}}{EV}) \approx 1.16\,\mathrm{deg}$. For Setup-B the modulation margin is given by $M = 0.44$ with $V_{dc} = 2.9\,\mathrm{pu}$. The pre-incident current margin with respect to the ratings of the semiconductors is calculated by $M_c = 1 - \frac{I_0}{I_{rat}} = 0.89$, where I_0 is the pre-incident phase current and I_{rat} the rated current of the semiconductors. For E1, the voltage sag is applied instantaneously.

3) Limitations of the chosen contingency scenarios

The considered scenarios in this study represent balanced grid disturbances. Due to the considered control architectures using PI controllers in dq-frame, the comparability with the $\alpha\beta$-frame controller only holds for the positive sequence [26], [38] and consequently only for balanced conditions and faults. To ensure comparability under unbalanced conditions, more complex approaches for the dq-frame control would be needed to fairly handle negative-sequence components [34], e.g., found in [39], [40], which is out of scope for our considerations.

4) Performances metrics

The following metrics are based on the measurement of the capacitor voltage of the grid connection filter and the filter inductor current as depicted in Fig. 1.

- M1) *Short-term voltage support:* To assess the fast-timescale impact on the voltage, we consider the normalized rms voltage of the three phases during the first 10 cycles following the event

$$V_{\mathrm{rms}}^{10c} = \frac{1}{V_{\mathrm{base}}}\left(\sqrt{\frac{1}{3\,N}\sum_{n=1}^{N}(v_{ga,n}^2 + v_{gb,n}^2 + v_{gc,n}^2)}\right) \,,$$

where the additional index a, b, c denotes phase and N the number of considered samples, which are chosen to reflect 10 cycles of the nominal frequency.

M2) *Nadir voltage:* To quantify the voltage nadir following each incident, we consider the smallest absolute value of a peak or valley in the 5 cycles following the considered event, referred to as $V_{p,min}^{5c}$, which is calculated as

$$V_{p,min}^{5c} = \frac{1}{V_{\text{base}}} \min(v_{ga,p}, v_{gb,p}, v_{gc,p}) \,,$$

where the phase peaks $v_{ga,p}$, $v_{gb,p}$, $v_{gc,p}$ are obtained by using the MATLAB function *findpeaks*[1] on the absolute values of the sampled data for the respective phase voltages. Please note that the choice of V_{base} for the normalization yields pu values above 1 for nominal conditions.

M3) *Settling time:* The settling time $T_{\text{set}}^{x\%}$ is defined as the post-incident time from which on the rms apparent power remains within $\pm x\%$ of the new steady state value.

M4) *Oscillation index:* The post-incident oscillation is quantified by the number of times the apparent power response changes direction, N_{osc}, during the settling time.

M5) *Maximum current following the incident:* To quantify the degree of the response to an incident, the maximum current $I_{\max}$ is considered as a metric. $I_{\max}$ refers to the largest instantaneous value of any phase currents.

M6) *Active power contribution:* To assess the active power injection for an event, we evaluate the normalized active power integral P_{int} for the duration of the event plus 10 cycles of the nominal frequency. For this, the filtered measurements of P are integrated via the trapezoidal rule, and the obtained value is normalized by the base energy $E_{\text{base}} = S_{\text{base}}\,1\,\text{s}$.

Regarding the above metrics, please note the following additions for traceability:

- *Power filter:* The power values for both setups are obtained by filtering the instantaneous values using a first-order low-pass filter with a cutoff frequency of $100\,\text{Hz}$.
- *Post-incident steady-state:* in this context, post-incident steady-state apparent power is defined as the mean value of the last $20\,\text{ms}$ of filtered apparent power measurements. For experiments E1 and E2, a duration of $1\,\text{s}$ is recorded and for E3, $2\,\text{s}$, allowing for all event-induced transients to settle.
- *Settling threshold:* For E3 a $3\,\%$ settling threshold is used instead of the $5\,\%$ as for E1 and E2, because the post-event dynamics for E3 are within the $5\,\%$ band and thus the post-incident oscillation index as well as the settling time were not capturing the observed behavior.
- *Procedure N_{osc} Setup-B:* To obtain a meaningful oscillation index for noisy measurements, the following post-processing procedure is used for the Setup-B results: the MATLAB filter function *smoothdata*[2] is applied to the sample-based difference of the apparent power measurement with a Gaussian weighted average with a window length of 250 samples. Then the sign changes of the resulting vector are counted to obtain N_{osc}. No minimum separation or prominence is demanded.

[1]https://www.mathworks.com/help/signal/ref/findpeaks.html

B. Test Setups

Two complementary test setups are used to evaluate the influences of control architecture during the described contingency scenarios. The two systems are not intended as hardware–simulation replicas. Instead, they span a broader range of practical configurations and evaluate the robustness of the results across different setups. Their pu values are within the typical range for grid-connected inverters, consistent with observations in practical systems.

1) Setup-A: Simulations

Setup-A is based on simulations using a MATLAB/Simulink implementation of the system under study, as shown in Fig. 14. The parameters are based on the benchmark system

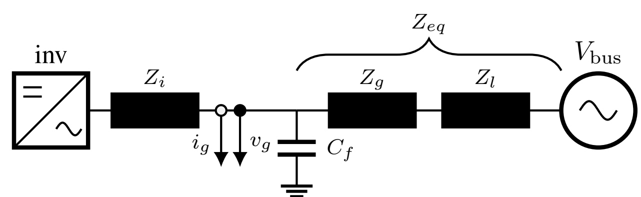

FIGURE 14. Schematic overview of Setup-A (simulation), including the inverter (inv), the relevant impedance of the grid connection LCL-filter $Z_i = R_i + j\,X_i$, $Z_g = R_g + j\,X_g$, the line impedance $Z_l = R_l + j\,X_l$, and the infinite bus voltage source (V_{bus}). Further, it illustrates the voltages and currents used to calculate the derived values. The inverter switching frequency is 20 kHz.

used in [41]. For the parameters, please refer to Table 1. The inverter under consideration is connected to the grid via an LCL filter. The control system runs at $f_s = 20\,\text{kHz}$, introducing realistic sampling and actuation delays. A simulation timestep of $t_{\text{sim}} = 1/(100 f_s)$, i.e., a sampling time of $500\,\text{ns}$ is chosen, and the inverter is implemented as an averaged model. Note that using an averaged model for the inverter omits PWM generation and switching transients. This approach is deliberate, as the study aims to examine the influence of control architecture and implementation, rather than hardware-specific details.

Designed as a simulation setup, the results are easily reproducible, and hardware-specific effects can be deliberately excluded.

[2]https://de.mathworks.com/help/releases/R2024b/matlab/ref/smoothdata.html

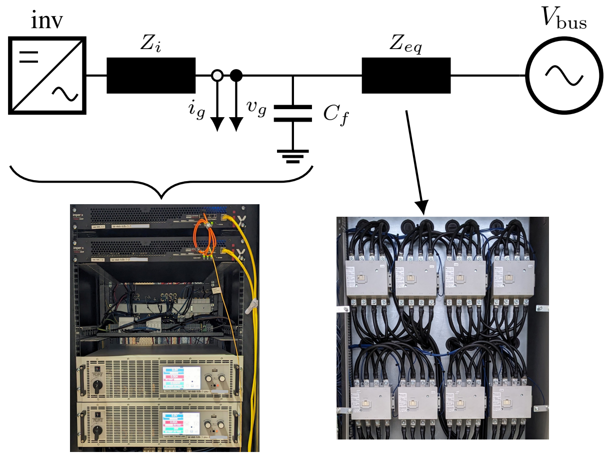

FIGURE 15. Schematic overview of Setup-B, including the inverter (inv), the relevant impedance of the grid connection LC-filter $Z_i = R_i + jX_i$, the equivalent impedance $Z_{eq} = R_{eq} + jX_{eq}$, and the infinite bus voltage source (V_{bus}). Further, it illustrates the voltages and currents used to calculate the derived values. The inverter switching frequency is 50 kHz.

2) Setup-B: Hardware Tests

Setup-B is a hardware setup consisting of two programmable inverters [42], interconnected by a transmission-line replica [43]. One inverter is operated as the inverter under test (inv) programmed with the various grid-forming controls under study, and the other is operated in an open-loop fashion to represent the stiff voltage bus (V_{bus}), see Fig. 15. Both systems are supplied by independent DC supplies (not illustrated). The control and switching frequency of the inverter under study is $50\,\mathrm{kHz}$. To compensate for slight DC offsets in the voltage and current measurements, which introduce harmonic content in the derived power, the measurements used for power calculations are high-pass filtered with a first-order filter with a cut-off frequency of $0.5\,\mathrm{Hz}$. Because of the hardware implementation, this setup accounts for real-world effects such as sampling, time delays, switching, and measurement/sensor effects.

3) Comparison of the test setups

Setup-A (simulation-based) and Setup-B (hardware-based) cover a broad range of typical configurations and parameters, as well as real-world effects such as sampling/control delays and measurement effects (Setup-B). Still, both are based on the single-inverter-to-infinite-bus setup to obtain reproducibility and provide insights. For this, they differ in the following key parameters:

- *Grid connection:* Different X_{eq}/R_{eq} ratios of the connection to the infinite bus. Setup-A is mainly inductive with an X_{eq}/R_{eq} ratio of 15.6, and Setup-B is a less inductive grid with an $X_{eq}/R_{eq} = 7.4$. Note that these differences result in different steady-state power flows for the same grid congestion scenario.
- *Grid base values:* the base frequency of Setup-A is $60\,\mathrm{Hz}$ compared to $50\,\mathrm{Hz}$ for Setup-B. This is reflected in the control design, where the base frequency serves as a reference for the current and voltage control bandwidths. Further, the baseline phase-to-neutral voltage of Setup-A is $9.24\,\mathrm{V}$ and $100\,\mathrm{V}$ for Setup-B. For the base currents $1.15\,\mathrm{A}$ for Setup-A is chosen and $17.3\,\mathrm{A}$ for Setup-B. The base impedances are given by $8.0\,\Omega$ and $5.8\,\Omega$ for Setup-A and Setup-B, respectively.
- *Grid connection filter:* Setup-A uses an LCL filter, whereas Setup-B uses an LC filter. Further, the inverter-side inductor and capacitor values differ in their respective per-unit systems. This is reflected in the control design, where we consider the nominal values.
- *Short circuit ratio (SCR):* For the two setups, the following SCRs result according to

$$\mathrm{SCR} = \frac{S_g}{S_n} = \frac{V_{LL}^2}{|Z_{eq}|\,S_n}\,, \tag{31}$$

where S_g is the short-circuit apparent power at the PCC and $\mathrm{S_{inv}}$ is the nominal inverter power and V_{LL} the nominal line-line voltage. This yields an SCR of 13.01 for Setup-A and 9.84 for Setup-B.

Note that the differences in parameters, such as grid base frequency or inverter-side inductor values, are considered

TABLE 2. Overview of controller parameters for Setup-A and Setup-B in the respective pu system.

Parameter	Setup-A	Setup-B	Description
$k_p^{\alpha\beta}$	$11.6 \cdot 10^{-2}$	1.03	proportional gain $\alpha\beta$-CC
$k_r^{\alpha\beta}$	$5.12 \cdot 10^{4}$	$1.05 \cdot 10^{5}$	resonant gain $\alpha\beta$-CC
ω_c	$8 \cdot 10^{-6}$	$1.6 \cdot 10^{-6}$	resonant width $\alpha\beta$-CC
$p_{g,cc}$	$2 \cdot 10^{6}$	$2 \cdot 10^{6}$	peak gain $\alpha\beta$-CC
k_p^{dq}	$11.3 \cdot 10^{-2}$	1.03	proportional gain dq-CC
k_i^{dq}	0.5	0.19	integral gain dq-CC
$k_{p,vc}^{\alpha\beta}$	$6.07 \cdot 10^{-2}$	$4.8 \cdot 10^{-2}$	proportional gain $\alpha\beta$-VC
$k_{r,vc}^{\alpha\beta}$	$1.51 \cdot 10^{5}$	$2.4 \cdot 10^{5}$	resonant gain $\alpha\beta$-VC
$\omega_{c,vc}$	$1.06 \cdot 10^{-5}$	$3.18 \cdot 10^{-6}$	resonant width $\alpha\beta$-VC
$p_{g,vc}$	$5 \cdot 10^{6}$	$10 \cdot 10^{6}$	peak gain $\alpha\beta$-VC
$k_{p,vc}^{dq}$	0.3	0.24	proportional gain dq-VC
$k_{i,vc}^{dq}$	1.51	1.2	integral gain dq-VC
L_{v}	0.251	0.44	virtual inductance
R_{v}	0.05	0.09	virtual resistance
ω_0	1	1	nominal angular frequency
V_0	1	1	nominal voltage amplitude
k_{Pf}	0.05	0.05	P/f droop
k_{QV}	$4.1 \cdot 10^{-2}$	$4.1 \cdot 10^{-2}$	Q/V droop
k_p	$1.13 \cdot 10^{-2}$	$1.84 \cdot 10^{-2}$	VSM damping factor
k_i	$2.7 \cdot 10^{-3}$	$3.2 \cdot 10^{-3}$	VSM inertia factor
k_g	$5.3 \cdot 10^{-2}$	$6.4 \cdot 10^{-2}$	VSM droop factor

TABLE 3. Alternative tuning parameters for the parameter influence study.

Controller	$p_{g,cc}$	ω_c	H	Description
D-VA-$\alpha\beta$-t1	$2 \cdot 10^{6}$	$1.06 \cdot 10^{-5}$ pu	–	baseline
D-VA-$\alpha\beta$-t2	$2 \cdot 10^{3}$	$1.33 \cdot 10^{-4}$ pu	–	lower resonant peak
D-VA-$\alpha\beta$-t3	$1 \cdot 10^{3}$	$1.33 \cdot 10^{-4}$ pu	–	lowest resonant peak
VSM-VA-$\alpha\beta$	–	–	0.5 s	baseline
VSM-VA-$\alpha\beta$-h	–	–	1 s	doubled inertia

TABLE 4. Voltage sag scenario (E1) performance metrics for Setup-A. The baseline (D-VA-$\alpha\beta$-t1) is given by $V_{\text{rms}}^{10c} = 0.842\,\text{pu}$, $V_{p,\text{min}}^{5c} = 1.178\,\text{pu}$, $T_{\text{set}} = 52.7\,\text{ms}$, $I_{\text{max}} = 1.54\,\text{pu}$, $P_{\text{int}} = 0.05\,\text{pu}$.

Control	V_{rms}^{10c}	$T_{\text{set}}^{5\%}$	I_{max}	N_{osc}	$V_{\text{p,min}}^{5c}$	P_{int}
D-VA-$\alpha\beta$-t1	100.0 %	100.0 %	100.0 %	5	100.0 %	100.0 %
D-VA-dq	100.0 %	115.0 %	91.3 %	6	98.0 %	100.0 %
D-VC-$\alpha\beta$	100.0 %	262.1 %	78.9 %	31	99.3 %	101.3 %
D-VC-dq	99.9 %	206.9 %	82.4 %	6	97.9 %	101.8 %
VSM-VA-$\alpha\beta$	100.0 %	102.1 %	101.0 %	5	100.0 %	99.3 %
VSM-VC-$\alpha\beta$	100.0 %	288.1 %	79.0 %	29	99.3 %	100.8 %
VSM-VA-$\alpha\beta$-h	100.0 %	102.2 %	100.6 %	5	100.0 %	98.7 %
D-VA-$\alpha\beta$-t2	101.2 %	736.0 %	149.3 %	12	103.4 %	105.1 %
D-VA-$\alpha\beta$-t3	102.6 %	1472.3 %	151.5 %	10	105.2 %	113.8 %

TABLE 5. Voltage sag scenario (E1) performance metrics for Setup-B. The baseline (D-VA-$\alpha\beta$-t1) is given by $V_{\text{rms}}^{10c} = 0.837\,\text{pu}$, $V_{p,\text{min}}^{5c} = 1.175\,\text{pu}$, $T_{\text{set}} = 62.9\,\text{ms}$, $I_{\text{max}} = 0.823\,\text{pu}$, $P_{\text{int}} = 0.043\,\text{pu}$.

Control	V_{rms}^{10c}	$T_{\text{set}}^{5\%}$	I_{max}	N_{osc}	$V_{\text{p,min}}^{5c}$	P_{int}
D-VA-$\alpha\beta$-t1	100.0 %	100.0 %	100.0 %	5	100.0 %	100.0 %
D-VA-dq	99.7 %	69.5 %	97.0 %	5	99.9 %	99.0 %
D-VC-$\alpha\beta$	100.0 %	177.1 %	84.9 %	14	99.3 %	100.8 %
D-VC-dq	100.0 %	69.6 %	82.5 %	1	100.1 %	100.9 %
VSM-VA-$\alpha\beta$	100.0 %	99.7 %	100.1 %	5	100.2 %	100.6 %
VSM-VC-$\alpha\beta$	100.0 %	105.5 %	84.8 %	7	99.1 %	101.1 %
VSM-VA-$\alpha\beta$-h	100.1 %	102.5 %	100.0 %	5	100.1 %	102.3 %
D-VA-$\alpha\beta$-t2	100.4 %	197.0 %	101.5 %	11	100.4 %	108.9 %
D-VA-$\alpha\beta$-t3	100.4 %	160.5 %	100.8 %	9	100.2 %	109.0 %

explicitly in the control design, such that no systematic difference is introduced. Table 2 summarizes the resulting control parameters for the setups.

4) Tuning variants for parameter study

To study the influence of tuning parameters, the tuning variants D-VA-$\alpha\beta$-t2 and D-VA-$\alpha\beta$-t3 denote alternative tunings of the current-control peak shape for PR-based current control. Both tuning alternatives use lower resonant peak gains $p_{g,cc}$ for current control and a wider resonant peak ω_c, which reshapes the resonant peak and yields a less aggressive, slower response. Note that the designed control bandwidth remains unchanged. For the VSM-based primary control, VSM-VA-$\alpha\beta$-h describes a version with doubled inertia. The parameters of these controllers that differ from their respective values in Table 2 are summarized in Table 3, along with the corresponding baseline values.

C. Results of the Simulation and Hardware Experiments

1) Results of voltage sag scenario (E1)

Table 4 summarizes the performance metrics for the voltage sag scenario E1 for Setup-A, and Table 5 summarizes them for Setup-B. All values are normalized using the respective D-VA-$\alpha\beta$-t1 values as a baseline.

For the considered performance metrics, we observe the following:

- *Voltage support V_{rms}^{10c}:* The values range between 99.7 % and 102.6 % across both setups. Notably, the voltage support for the D-VA-$\alpha\beta$-t2 and D-VA-$\alpha\beta$-t3 has increased. The spread is larger for the more inductive grid connection (Setup-A), as expected due to the greater impact of reactive power injection.
- *Voltage nadir $V_{\text{p,min}}^{5c}$:* Obtained values range between 97.9 % and 105.2 %. Again, D-VA-$\alpha\beta$-t2 and D-VA-$\alpha\beta$-t3 yield improved voltage support in both experiment setups.
- *Settling time $T_{\text{set}}^{5\%}$:* The settling time ranges between 69.5 % and 1472.3 %, where again Setup-A shows a larger spread of the values.
- *Oscillation index N_{osc}:* The oscillation index ranges between 5 and 38. The D-VC-$\alpha\beta$ implementation shows the least damped response. For the more inductive grid, the oscillation is more pronounced across all conducted experiments.
- *Maximum current I_{max}:* The values range between 78.9 % and 151.5 %. Notable is that decreased maximum current corresponds with decreased $V_{\text{p,min}}^{5c}$, however not V_{rms}^{10c}.
- *Active power injection P_{int}:* Values between 98.7 % and 113.8 % were obtained. As expected, increased power injection corresponds to increased voltage support at the cost of increased settling time.

2) Results of the phase angle jump scenario (E2)

For the phase angle jump scenario E2, the resulting performance metrics are presented in Table 6 for Setup-A and in Table 7 for Setup-B. Again, all values are normalized using the respective D-VA-$\alpha\beta$-t1 results as the baseline.

For the considered performance metrics, we observe the following:

- *Voltage support V_{rms}^{10c}:* The values range between 99.6 % and 100.1 %. In this scenario, D-VA-$\alpha\beta$-t2 and D-VA-$\alpha\beta$-t3 yield less voltage support in both experiment setups.
- *Voltage nadir $V_{\text{p,min}}^{5c}$:* Obtained values range between 99.8 % and 102.3 %. Notably, the dq implementations yield larger values in both setups.
- *Settling time $T_{\text{set}}^{5\%}$:* The settling time ranges between 71.4 % and 180.0 %. In both setups, tuning with increased inertia yields significantly longer settling times, as expected. The spread of values for Setup-A is smaller compared to the more resistive Setup-B.

TABLE 6. Phase angle jump scenario (E2) performance metrics for Setup-A. The baseline (D-VA-$\alpha\beta$-t1) is given by $V_{\text{rms}}^{10c} = 0.996\,\text{pu}$, $V_{p,\text{min}}^{5c} = 1.357\,\text{pu}$, $T_{\text{set}} = 247\,\text{ms}$, $I_{\text{max}} = 1.93\,\text{pu}$, $P_{\text{int}} = 0.06\,\text{pu}$.

Control	V_{rms}^{10c}	$T_{\text{set}}^{5\%}$	I_{max}	N_{osc}	$V_{\text{p,min}}^{5c}$	P_{int}
D-VA-$\alpha\beta$-t1	100.0 %	100.0 %	100.0 %	6	100.0 %	100.0 %
D-VA-dq	100.0 %	99.9 %	95.4 %	8	101.8 %	99.8 %
D-VC-$\alpha\beta$	99.9 %	100.3 %	84.5 %	38	101.5 %	100.0 %
D-VC-dq	99.9 %	101.1 %	79.6 %	6	102.3 %	100.4 %
VSM-VA-$\alpha\beta$	100.0 %	98.4 %	99.8 %	9	100.0 %	97.3 %
VSM-VC-$\alpha\beta$	99.9 %	103.7 %	83.0 %	37	101.5 %	97.5 %
VSM-VA-$\alpha\beta$-h	100.0 %	180.0 %	99.8 %	8	100.0 %	99.5 %
D-VA-$\alpha\beta$-t2	99.9 %	100.2 %	133.3 %	7	99.9 %	101.6 %
D-VA-$\alpha\beta$-t3	99.8 %	123.1 %	135.2 %	8	99.8 %	102.4 %

TABLE 7. Phase angle jump scenario (E2) performance metrics for Setup-B. The baseline (D-VA-$\alpha\beta$-t1) is given by $V_{\mathrm{rms}}^{10c} = 1.0\,\mathrm{pu}$, $V_{p,\mathrm{min}}^{5c} = 1.4\,\mathrm{pu}$, $T_{\mathrm{set}} = 262\,\mathrm{ms}$, $I_{\max} = 0.86\,\mathrm{pu}$, $P_{\mathrm{int}} = 0.05\,\mathrm{pu}$.

Control	V_{rms}^{10c}	$T_{\mathrm{set}}^{5\%}$	$I_{\max}$	N_{osc}	$V_{\mathrm{p,min}}^{5c}$	P_{int}
D-VA-$\alpha\beta$-t1	100.0 %	100.0 %	100.0 %	17	100.0 %	100.0 %
D-VA-dq	100.1 %	74.0 %	94.6 %	14	100.5 %	100.5 %
D-VC-$\alpha\beta$	99.9 %	96.3 %	87.8 %	29	100.0 %	99.4 %
D-VC-dq	99.9 %	71.4 %	88.3 %	18	100.4 %	100.2 %
VSM-VA-$\alpha\beta$	100.0 %	89.4 %	99.2 %	14	100.3 %	101.5 %
VSM-VC-$\alpha\beta$	100.0 %	84.1 %	85.5 %	14	99.8 %	101.1 %
VSM-VA-$\alpha\beta$-h	100.1 %	176.2 %	99.5 %	41	100.9 %	107.3 %
D-VA-$\alpha\beta$-t2	99.7 %	74.4 %	102.4 %	10	99.8 %	100.6 %
D-VA-$\alpha\beta$-t3	99.6 %	74.2 %	104.8 %	10	100.3 %	100.5 %

- *Oscillation index N_{osc}:* The oscillation index ranges between 6 and 57. In both setups, the PI/PR-based voltage control yields a less-damped response, especially in Setup-A.
- *Maximum current $I_{\max}$:* The values range between 79.6 % and 135.2 %. Notably, the dq-frame approaches, as well as PI/PR-based voltage control, yield smaller maximum currents in both setups.
- *Active power injection P_{int}:* Values between 98.7 % and 113.8 % were obtained. As expected, increased power injection corresponds to increased voltage support.

3) Results of the ROCOF scenario (E3)

For the ROCOF scenario (E3), the performance metrics for Setup-A are summarized in Table 8 and for Setup-B in Table 9. Again, all values are normalized using the results of the respective D-VA-$\alpha\beta$-t1.

For the considered performance metrics, we observe the following:

- *Voltage support V_{rms}^{10c}:* The values range between 98.7 % and 100.2 %. In this scenario, D-VA-$\alpha\beta$-t2 and D-VA-$\alpha\beta$-t3 yield the smallest values for V_{rms}^{10c}.
- *Voltage nadir $V_{\mathrm{p,min}}^{5c}$:* The obtained values range between 99.1 % and 100.1 %. Compared to the other scenarios, the range is smaller, as expected given the continuous nature of this scenario.
- *Settling time $T_{\mathrm{set}}^{3\%}$:* The settling time ranges between 93.5 % and 484.3 %. The increased inertia controller VSM-VA-$\alpha\beta$-h yields the longest settling time in both setups.
- *Oscillation index N_{osc}:* The oscillation index ranges between 1 and 3. Due to the continuous nature of this scenario, the range of N_{osc} is small, and the differences are due to differences in the overshoot after the end of the ROCOF event.
- *Maximum current $I_{\max}$:* The values range between 98.8 % and 116.6 %. Notably, an increase in maximum current does not correspond to active power support. Especially for D-VA-$\alpha\beta$-t2 and D-VA-$\alpha\beta$-t3, the increased current does not yield improved P_{int} or V_{rms}^{10c}.
- *Active power injection P_{int}:* Values between 99.0 % and 108.5 % were obtained. The most notable increase occurs in the high-inertia controller tuning VSM-VA-$\alpha\beta$-h for both setups, as expected.

D. Influence of Reference Frame

The obtained performance metrics show that the choice of reference frame affects the fast-timescale behavior. Notable influences are:

- *Oscillation index N_{osc}:* for the PI/PR-based voltage control architectures, the oscillation index shows a strong dependency where the dq-frame-based control shows a better damped response. This can be clearly seen by the results of the voltage step scenario (E1) in Fig. 16 for Setup-A and in Fig. 17 for Setup-B.
- *Settling time $T_{\mathrm{set}}^{5\%}$:* For Setup-B, the dq-frame realizations yield significantly faster $T_{\mathrm{set}}^{5\%}$; this is not observed for Setup-A, where the range of settling times is smaller. Even without a clear trend, the influence is clearly visible.
- *Nadir voltage $N_{\mathrm{p,min}}^{5c}$:* In both step-change scenarios E1 and E2, the $V_{\mathrm{p,min}}^{5c}$ values depend on the reference frame. For E1, the direction of the dependency depends on the setup. For E2, the dq-frame architectures yield improved values for both setups.

Note that the results can differ significantly under unbalanced conditions, which are out of scope for the present study. In the following, we analyze and discuss the causes of this behavior.

TABLE 8. ROCOF scenario (E3) performance metrics for Setup-A. The baseline (D-VA-$\alpha\beta$-t1) is given by $V_{\mathrm{rms}}^{10c} = 0.991\,\mathrm{pu}$, $V_{p,\mathrm{min}}^{5c} = 1.400\,\mathrm{pu}$, $T_{\mathrm{set}} = 38.5\,\mathrm{ms}$, $I_{\max} = 1.25\,\mathrm{pu}$, $P_{\mathrm{int}} = 0.42\,\mathrm{pu}$.

Control	V_{rms}^{10c}	$T_{\mathrm{set}}^{3\%}$	$I_{\max}$	N_{osc}	$V_{\mathrm{p,min}}^{5c}$	P_{int}
D-VA-$\alpha\beta$-t1	100.0 %	100.0 %	100.0 %	1	100.0 %	100.0 %
D-VA-dq	100.0 %	98.7 %	99.9 %	1	100.0 %	99.9 %
D-VC-$\alpha\beta$	99.8 %	99.6 %	101.5 %	1	99.8 %	99.9 %
D-VC-dq	99.8 %	108.2 %	101.9 %	1	99.8 %	99.9 %
VSM-VA-$\alpha\beta$	100.0 %	165.9 %	101.8 %	1	100.0 %	101.8 %
VSM-VC-$\alpha\beta$	99.8 %	171.0 %	103.3 %	1	99.8 %	101.7 %
VSM-VA-$\alpha\beta$-h	99.9 %	539.9 %	108.3 %	2	99.9 %	108.5 %
D-VA-$\alpha\beta$-t2	99.6 %	100.4 %	102.3 %	1	99.5 %	100.0 %
D-VA-$\alpha\beta$-t3	99.3 %	385.1 %	106.0 %	3	99.1 %	99.9 %

TABLE 9. ROCOF scenario (E3) performance metrics for Setup-B. The baseline (D-VA-$\alpha\beta$-t1) is given by $V_{\mathrm{rms}}^{10c} = 1.02\,\mathrm{pu}$, $V_{p,\mathrm{min}}^{5c} = 1.41\,\mathrm{pu}$, $T_{\mathrm{set}} = 76\,\mathrm{ms}$, $I_{\max} = 1.26\,\mathrm{pu}$, $P_{\mathrm{int}} = 0.49\,\mathrm{pu}$.

Control	V_{rms}^{10c}	$T_{\mathrm{set}}^{3\%}$	$I_{\max}$	N_{osc}	$V_{\mathrm{p,min}}^{5c}$	P_{int}
D-VA-$\alpha\beta$-t1	100.0 %	100.0 %	100.0 %	1	100.0 %	100.0 %
D-VA-dq	100.0 %	102.8 %	98.9 %	1	100.0 %	99.2 %
D-VC-$\alpha\beta$	99.8 %	120.0 %	100.7 %	1	99.4 %	100.0 %
D-VC-dq	99.9 %	95.0 %	98.8 %	1	100.1 %	99.5 %
VSM-VA-$\alpha\beta$	100.0 %	138.4 %	101.1 %	1	99.7 %	100.6 %
VSM-VC-$\alpha\beta$	99.8 %	142.4 %	101.8 %	1	99.6 %	100.6 %
VSM-VA-$\alpha\beta$-h	100.2 %	407.8 %	106.9 %	2	99.6 %	105.8 %
D-VA-$\alpha\beta$-t2	98.7 %	117.5 %	115.8 %	1	99.8 %	99.0 %
D-VA-$\alpha\beta$-t3	98.7 %	132.4 %	116.6 %	1	99.4 %	99.1 %

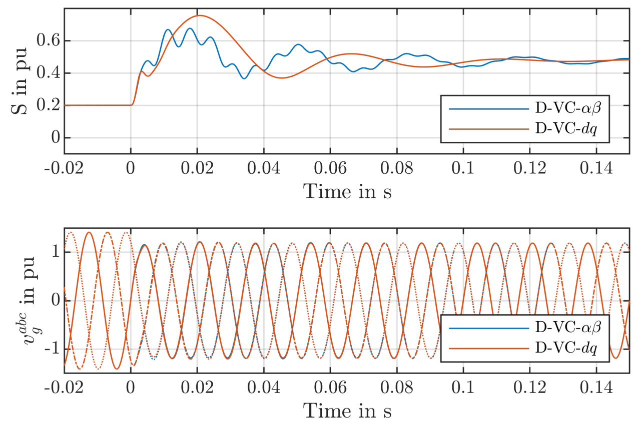

FIGURE 16. Comparison of D-VC-$\alpha\beta$ and D-VC-dq for E1 in Setup-A showing the influence of the chosen reference frame for PI/PR-based voltage control. The different line styles represent the phases; S denotes the apparent power.

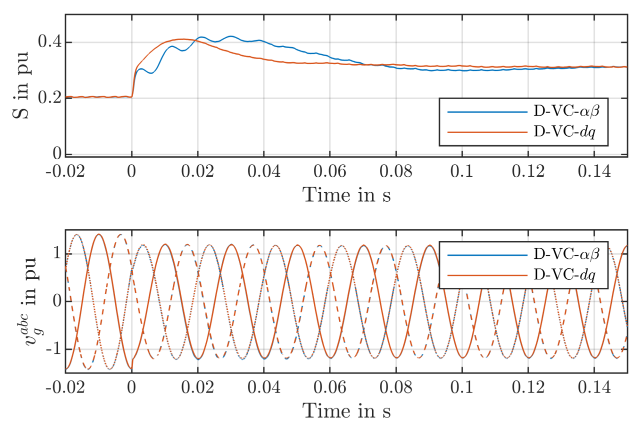

FIGURE 17. Comparison of D-VC-$\alpha\beta$ and D-VC-dq for E1 in Setup-B showing the influence of the chosen reference frame for PI/PR-based voltage control. The different line styles represent the phases; S denotes the apparent power.

1) Assumptions and their limitations

Several assumptions during the design process of the respective controllers contribute to the observed differences in the disturbance response:

- *Bandwidth as tuning metric:* As indicated in Section II.B, the standard tuning approach via the desired control bandwidth is not suited to ensure equivalent behavior of controllers designed in dq and $\alpha\beta$ across all frequencies. Since the controller bandwidth is typically located away from the nominal grid frequency, the behavior-defining shape of the resonance peak can differ, even if the controllers have the same bandwidth. The control tuning used in this paper yields comparable shapes of the resonance peak in a narrow frequency band around the synchronous frequency, as shown in Figs. 8 and 12. However, disturbances are not limited to this frequency band and can therefore increase the visibility of the differences.
- *Assumption of decoupled axis and ideal knowledge of parameters:* The synchronous reference frame design in Section II.B is based on the assumption of decoupled dq-axes. To avoid derivative actions in the decoupling network, typically, static feedback is used. This yields a decoupling that is exact only for the synchronous frequency component in steady state; therefore, the behavior during dynamic grid states, such as disturbances, can differ. Considering the dynamics for the grid current i_g, as denoted in Fig. 1, yields:

$$\frac{\mathrm{d}i_g^{abc}}{\mathrm{d}t} = \frac{1}{L_i}\left(-v_g^{abc} - R_i i_g^{abc} + v_{\mathrm{mod}}^{abc}\right), \tag{32}$$

in natural coordinates. In dq-frame we obtain

$$\frac{\mathrm{d}i_g^{dq}}{\mathrm{d}t} = -\mathcal{D}(\dot\theta(t))i_g^{dq} + \frac{1}{L_i}(-v_g^{dq} - R_i i_g^{dq} + v_{\mathrm{mod}}^{dq}), \tag{33}$$

where the coupling term $\mathcal{D}(\dot\theta(t))$ is given by

$$\mathcal{D}(\dot\theta(t)) = \begin{bmatrix} 0 & -\dot\theta(t) \\ \dot\theta(t) & 0 \end{bmatrix}, \tag{34}$$

which couples the d and q axis depending on $\dot\theta(t)$. To compensate for this coupling with the control action v_{mod}^{dq}, it is necessary to know L_i and $\dot\theta(t)$. The latter is often approximated using ω_0, and L_i is typically assumed to agree with the nominal value. This yields reasonable decoupling in steady-state operation around the nominal frequency. However, decoupling does not hold during transients, contributing to differences between dq- and $\alpha\beta$-frame implementations.

2) Analysis of the different couplings to the angle dynamics

To analyze the influence of the coupling to the angle dynamics via the transformations, we consider Fig. 18 and Fig. 19, which show the control implementation in dq- and $\alpha\beta$-frame explicitly including the necessary transformations. As an exemplary case of all occurring transformations, we

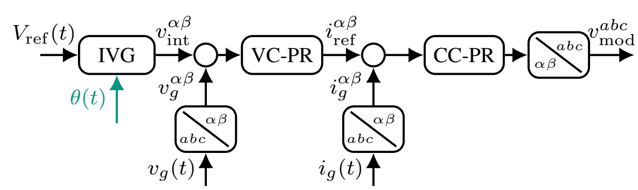

FIGURE 18. x-VC-$\alpha\beta$ control scheme including transformations, depicting the coupling to the synchronization mechanism.

analyze the measurement of the grid voltage. For the $\alpha\beta$-frame implementation we obtain:

$$v_g^{\alpha\beta} = \underbrace{\frac{2}{3}\begin{bmatrix} 1 & -\frac{1}{2} & -\frac{1}{2} \\ 0 & \frac{\sqrt{3}}{2} & -\frac{\sqrt{3}}{2} \end{bmatrix}}_{=:T_{\alpha\beta}} v_g\,, \tag{35}$$

which yields the following small signal model:

$$\Delta v_g^{\alpha\beta} = T_{\alpha\beta}\,\Delta v_g\,. \tag{36}$$

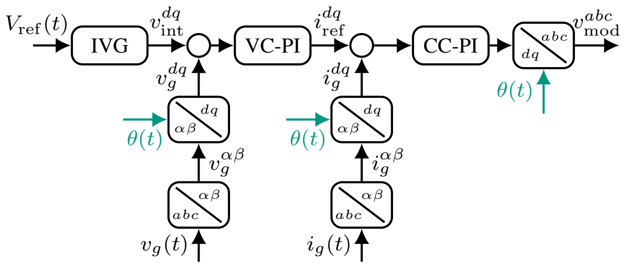

FIGURE 19. x-VC-dq control scheme including transformations, depicting the coupling to the synchronization mechanism.

We see that the Clarke Transformation $T_{\alpha\beta}$ does not depend on any other states such that no additional dynamics are introduced.

Considering the same for the dq-frame yields:

$$v_g^{dq} = \underbrace{\begin{bmatrix} \cos(\theta(t)) & \sin(\theta(t)) \\ -\sin(\theta(t)) & \cos(\theta(t)) \end{bmatrix}}_{=:T_{dq}(\theta(t))} v_g^{\alpha\beta}, \tag{37}$$

which yields the following small signal behavior:

$$\Delta v_g^{dq} = \underbrace{\begin{bmatrix} \text{-}\sin(\theta_e) & \cos(\theta_e) \\ \text{-}\cos(\theta_e) & \text{-}\sin(\theta_e) \end{bmatrix} v_e^{\alpha\beta}}_{\text{const.}} \Delta\theta + \underbrace{T_{dq}(\theta_e) T_{\alpha\beta}}_{\text{const.}} \Delta v_g, \tag{38}$$

where θ_e is the equilibrium angle around which the small-signal model is centered and $v_e^{\alpha\beta}$ is the corresponding grid voltage in $\alpha\beta$-frame. By comparing (36) and (38), it is clear that the dq transformation couples the angle dynamics $\Delta\theta$ and the grid voltage dynamics Δv_g to the voltage measurement. In contrast, the $\alpha\beta$ transformation only couples the voltage grid dynamics Δv_g to the voltage measurement.

Having established that the transformations yield different couplings to the angle/synchronization dynamics, we now discuss where these different couplings occur in the control architecture:

- *Reference path:* the angle dynamics in the $\alpha\beta$-frame implementation influence in the reference path via the IVG block, see Fig. 18. Whereas in the dq implementation, the reference path is influenced by the angle dynamics through the transformation generating the natural reference frame modulation voltage, see Fig. 19.
- *Measurement path:* For all obtained measurements, the dq transformation couples the angle dynamics to the measured values. This is inherent to methods based on rotating reference frames, since there exist two dq reference frames, the one of the IBR and the one of the grid. In steady-state operation, they are synchronized; however, during transient operation, they are subject to the synchronization dynamics defined in the primary control. The measurements in the $\alpha\beta$ case are not influenced by the angle dynamics.

3) Analysis of the disturbance attenuation

Considering the distinctly different disturbance response, we consider the disturbance transfer function as a comparison metric. Based on the model for the cascaded voltage control in Fig. 20, we study the influence of an exogenous disturbance of the grid voltage denoted by v_d. For the study of fast transients, we assume constant v_{int}. A disturbance of the

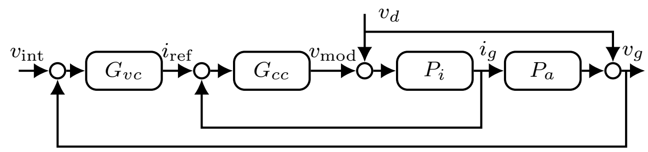

FIGURE 20. x-VC-xx control scheme including transformations and plants for the disturbance attenuation analysis.

capacitor voltage acts as an input disturbance for the inner plant $P_i = \frac{1}{sL_i+R_i}$ as well as an output disturbance for the outer plant $P_a = \frac{1}{sC_f}$. We obtain the following disturbance transfer function as:

$$\frac{\hat{v}_g(s)}{\hat{v}_d(s)} = \frac{1 + P_i(s)G_{cc}(s) + P_i(s)P_a(s)}{1 + P_i(s)G_{cc}(s) + P_i(s)P_a(s)G_{cc}(s)G_{vc}(s)}. \tag{39}$$

The corresponding Bode-plot for (39) for dq- and $\alpha\beta$-frame realization is compared in Fig. 21, where the dq-frame realization is frequency shifted to the fundamental frequency [38] for comparability. The different disturbance responses

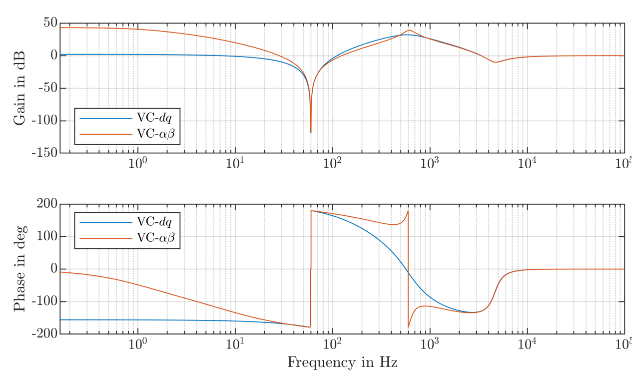

FIGURE 21. Bode plots of the disturbance transfer function, comparing the dq and $\alpha\beta$-frame implementations VC-dq and VC-$\alpha\beta$ using the parameters of Setup-A.

that can be observed in the time domain, for example, see Fig. 16 and Fig. 17, is also reflected in the frequency domain analysis. For disturbances below the nominal frequency, the capacitor-voltage response differs significantly. For disturbances at nominal frequency or above, these differences are smaller.

E. Impact of Voltage Control Architecture

The results show a clear influence of the chosen voltage control architecture on the response to the considered grid disturbances. Most notable are the differences regarding the following:

- *Settling time* $T_{\text{set}}^{5\%}$*:* For the voltage sag scenario E1 in both setups, the $\alpha\beta$ realization using virtual admittance control yields a significantly faster settling time. For the dq implementation, this is only observed for Setup-A, for Setup-B there is no significant difference. For the angle-related scenarios E2 and E3, this influence is not observed.
- *Oscillation index* N_{osc}*:* For the $\alpha\beta$ control implementations, the PR-based voltage controllers yield less damped responses for both step-change scenarios E1 and E2 in both setups.
- *Maximum current* I_{max}*:* The maximum current is reduced for the PI/PR-based voltage controllers in both experiment setups for both step-change scenarios, which is shown in Fig. 22 for E2 Setup-A and in Fig. 23 for E2 and Setup-B. In both setups, the virtual admittance implementations show a stronger initial overshoot yielding larger I_{max}.
- *Active power injection* P_{int}*:* For scenario E1, the PI/PR-based voltage controllers yield an increase in the injected active power for both setups.

By design, the virtual admittance-based control consists of fewer cascaded control loops, making the tuning easier. Further, since the voltage amplitude and possible harmonics are unregulated in a closed-loop sense, additional control loops are needed if such features are desired. The influence depends on the reference frame and the considered scenario. Even though the number of controller states differs between the virtual admittance and PI/PR-based voltage control, all considered controllers are either first- or second-order transfer functions that can be efficiently discretized such that, considering modern controller hardware, no significant influence on computational burden is expected.

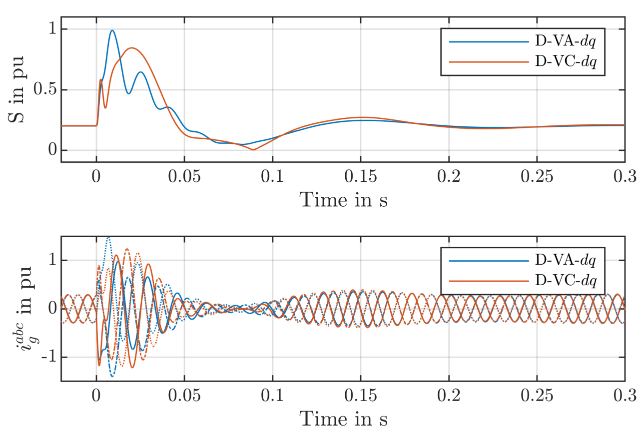

FIGURE 22. **Comparison D-VA-dq and D-VC-dq for Setup-A scenario E2, showing the difference between virtual admittance-based and PI-based voltage control in dq-frame. The different line styles represent the phases; S denotes the apparent power.**

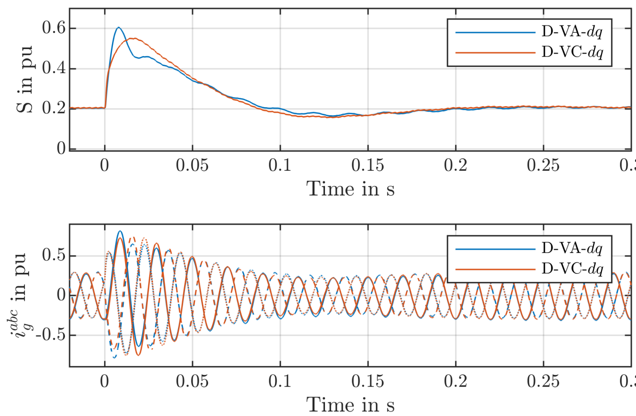

FIGURE 23. **Comparison D-VA-dq and D-VC-dq for Setup-B scenario E2, showing the difference between virtual admittance-based and PI-based voltage control in dq-frame. The different line styles represent the phases; S denotes the apparent power.**

TABLE 10. **Summary of controller architecture combinations, small-signal analysis, and experimental results.**

Property	D-VA-$\alpha\beta$	D-VA-dq	D-VC-$\alpha\beta$	D-VC-dq
Voltage controller	VA (2 states)	VA (2 states)	PR (4 states)	PI (2 states)
Current controller	PR (4 states)	PI (2 states)	PR (4 states)	PI (2 states)
Setup-A				
Stability	stable	stable	stable	stable
Dom. damping ζ^*	0.390	0.391	0.093	0.377
Range N_{osc} †	1–6	1–8	1–38	1–6
Disturbance Metrics: E1 Setup-A				
Osc modes excited	12	10	11	10
ζ^*_{osc}	0.400	0.420	0.229	0.381
Disturbance Metrics: E2 Setup-A				
Osc modes excited	13	11	12	11
ζ^*_{osc}	0.402	0.422	0.229	0.382
Setup-B				
Stability	stable	stable	stable	stable
Dom. damping ζ^*	0.540	0.590	0.519	0.589
Range N_{osc} $^{\dagger 1}$	1–17	1–14	1–29	1–18
Disturbance Metrics: E1 Setup-B				
Osc modes excited	13	10	14	9
ζ^*_{osc}	0.800	0.655	0.359	0.765
Disturbance Metrics: E2 Setup-B				
Osc modes excited	13	12	13	8
ζ^*_{osc}	0.592	0.485	0.417	0.536

*Small-signal eigenvalue analysis, varies with SCR (see Section III.G.2)
† Time-domain oscillation index N_{osc}, see Tables 4, 6, 8
$^{\dagger 1}$Time-domain oscillation index N_{osc}, see Tables 5, 7, 9

1) Analysis of the impact of voltage control architecture

The observed influence of the voltage control architecture for Setup-A and Setup-B is supported by small-signal analysis. Please refer to Appendix A for details on the small-signal model and metrics.

As summarized in Table 10, the control architecture contributes to the observed differences in disturbance response. PR controllers add four states versus two for PI or virtual admittance, increasing the system order and creating more excitable oscillatory modes. Considering the number of modes excited by the disturbances in Table 10 shows that the $\alpha\beta$ frame yields larger numbers.

However, more excitable modes do not necessarily produce more oscillation. The key factor is whether these modes are sufficiently damped. This is evident when comparing the performance of D-VA-dq and D-VA-$\alpha\beta$-t1 in Tables 4 – 7, where similar performance is achieved despite different numbers of excited modes.

The observation that D-VC-$\alpha\beta$ yields the highest oscillation metric N_{osc} during E1 and E2 is therefore consistent with the smallest reported dominant damping factors ζ as well as ζ_{osc} for weighted damping of the modes excited by the disturbance.

F. Influence of Primary Controller

One key feature of primary control schemes, such as droop control, is enabling parallel operation of multiple generation units. This is achieved by allowing power synchronization via an active power-to-frequency relationship inherent to synchronous generation units. Droop control, as given in (22), provides such a relation in steady state. Deploying a VSM-based primary control further allows shaping the transient behavior of the inverter during grid events by defining inertia and damping. Note that using a low-pass filter for power measurements in a droop-controlled system also introduces dynamics that exhibit inertia-like behavior. Therefore, we expect similar qualitative results for both primary control approaches. Since the compared primary controllers share the same reactive-power-voltage droop (see (23)), similar behavior is expected for the voltage sag scenario E1, which is observed for Setup-A and Setup-B, for the latter see Fig. 24. Influence is expected with respect to the angle-

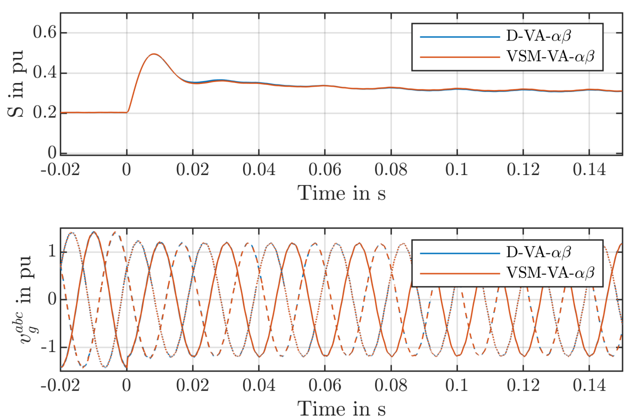

FIGURE 24. **Comparison D-VA-$\alpha\beta$ and VSM-VA-$\alpha\beta$ for Setup-B scenario E1, showing the lack of influence of primary control, since the scenario is purely voltage-related. The different line styles represent the phases. S denotes the apparent power.**

related scenarios E2 and E3, which is reflected in the obtained performance metrics:

- *Settling time* $T_{\mathrm{set}}^{3\%}$*:* For E2 (phase jump), the VSM-based primary control yields slightly faster settling times, whereas for E3, the VSM-based primary control yields increased settling times. Considering the results for E2, see Fig. 25 for Setup-A and Fig. 26 for Setup-B. We see that for the VSM approach, the response after the initial overshoot shows a better-damped decay to the steady state. However, the overall response shape is preserved. For E3, the time-domain results are similar despite the difference in $T_{\mathrm{set}}^{3\%}$ as shown in Fig. 27 for Setup-B.
- *Active power injection* P_{int}*:* For E2, the injected power differs for the VSM approach and the droop control for both setups, due to the differently damped response after the initial overshoot, as previously discussed.

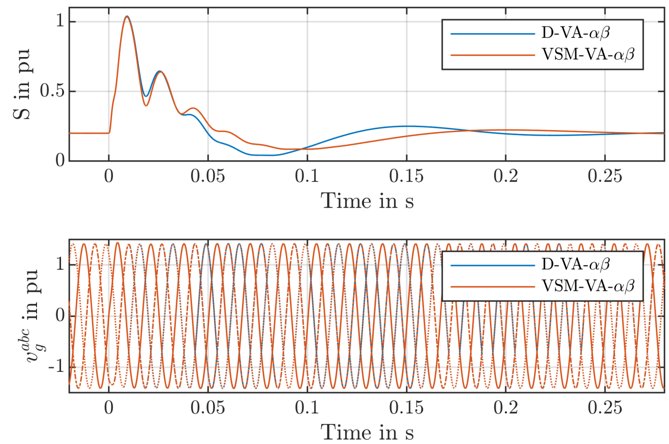

FIGURE 25. **Comparison D-VA-$\alpha\beta$ and VSM-VA-$\alpha\beta$ for Setup-A scenario E2, showing the difference in damping after the initial overshoot. The different line styles represent the phases; S denotes the apparent power.**

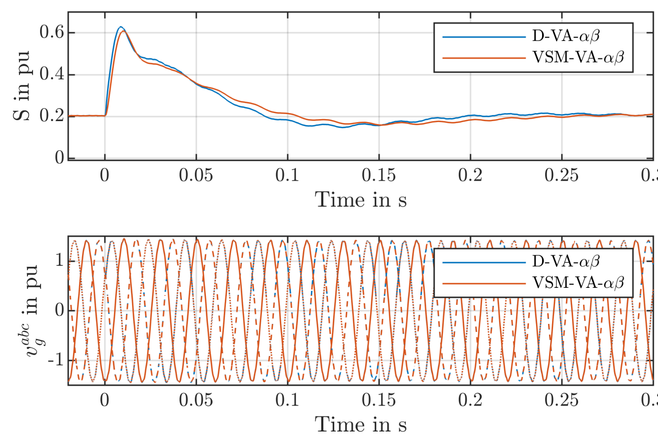

FIGURE 26. **Comparison D-VA-$\alpha\beta$ and VSM-VA-$\alpha\beta$ for Setup-B scenario E2, showing the difference in damping after the initial overshoot. The different line styles represent the phases. S denotes the apparent power.**

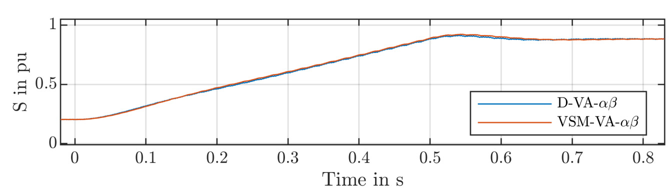

FIGURE 27. **Comparison D-VA-$\alpha\beta$ and VSM-VA-$\alpha\beta$ for Setup-B scenario E3. Despite the difference in $T_{\mathrm{set}}^{3\%}$, the time-domain behavior is similar. S denotes the apparent power.**

In summary, the influence of the primary control on the fast timescale is evident, though insignificant compared

This article has been accepted for publication in IEEE Open Journal of Power Electronics. This is the author's version which has not been fully edited and content may change prior to final publication. Citation information: DOI 10.1109/OJPEL.2026.3734120

to that of other control-architecture choices. Notably, the primary control's effect depends on interactions among angle dynamics, voltage dynamics, and power flow, all of which are strongly influenced by the grid's X/R ratio.

G. Sensitivity to Control Tuning and Grid Strength

To analyze the sensitivity of the tuning of the controllers on the results, we consider the following influences: (i) chosen bandwidth during the control design process, (ii) inertia for the VSM primary control implementation, and (iii) peak shape design for $\alpha\beta$-frame current controller.

1) Impact of chosen bandwidth during control design

To analyze the sensitivity to bandwidth in the control design, we consider the effects of a $20\,\%$ increase and a $20\,\%$ decrease in bandwidth. The baseline controllers are: D-VA-$\alpha\beta$-t1 and D-VC-$\alpha\beta$ in $\alpha\beta$-frame and D-VA-dq and D-VC-dq in dq-frame, as described in Section II.A and Table 2. For the adapted controller parametrization, the bandwidth of the current controller $\omega_{\mathrm{gc,cc}}$ is altered to $0.8\,\omega_{\mathrm{gc,cc}}$ or $1.2\,\omega_{\mathrm{gc,cc}}$, respectively. The remainder of the design procedure is unchanged to ensure the timescale separation between the control loops. Note that the additional design parameters of the PR controllers are kept constant.

For the voltage sag scenario E1, the influence of the control bandwidth in combination with the virtual admittance-based control in $\alpha\beta$-frame is depicted in Fig. 28 for Setup-A. The chosen bandwidth does not affect the qualitative

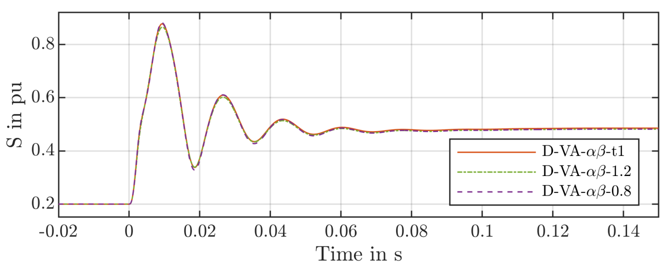

FIGURE 28. Comparison D-VA-$\alpha\beta$-t1 (baseline), D-VA-$\alpha\beta$-1.2 and D-VA-$\alpha\beta$-0.8 for E1 Setup-A showing the influence of different control bandwidths in the design process. S denotes the apparent power.

behavior. Quantitatively, increasing bandwidth yields slightly better damping and reduced overshoot. Overall, the influence of bandwidth in this configuration is minimal.

The same holds for the virtual admittance-based implementation in dq-frame, which is presented in Fig. 29 for Setup-A. Again, increasing the current controller bandwidth slightly improves damping, while the qualitative behavior remains unchanged.

We now consider the results for the PI/PR-based voltage control schemes. Fig. 30 compares the results for the $\alpha\beta$-frame architecture.

Again, bandwidth does not affect qualitative behavior, and increasing it yields a slightly better-damped response.

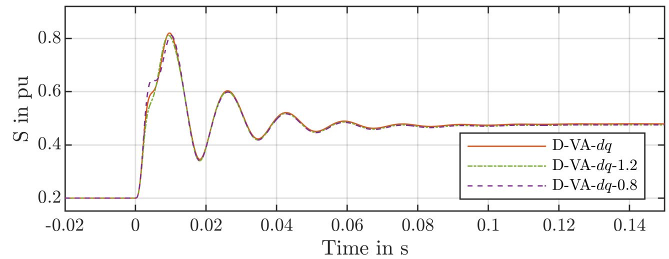

FIGURE 29. Comparison D-VA-dq (baseline), D-VA-dq-1.2, and D-VA-dq-0.8 for E1 Setup-A showing the influence of different control bandwidths in the design process. S denotes the apparent power.

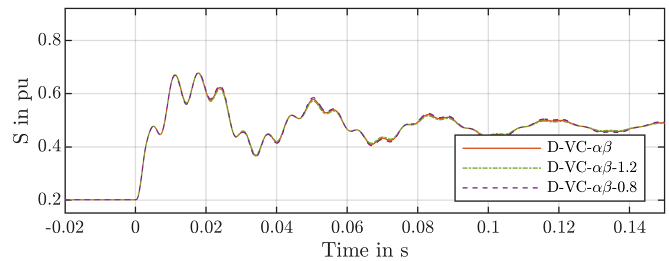

FIGURE 30. Comparison D-VC-$\alpha\beta$ (baseline), D-VC-$\alpha\beta$-1.2 and D-VC-$\alpha\beta$-0.8 for E1 Setup-A showing the influence of different control bandwidths in the design process. S denotes the apparent power.

For the corresponding dq-frame implementation of the PI-based voltage control scheme, the results are depicted in Fig. 31.

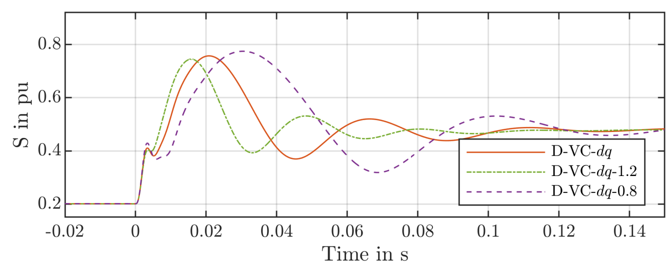

FIGURE 31. Comparison D-VC-dq (baseline), D-VC-dq-1.2, and D-VC-dq-0.8 for E1 Setup-A showing the influence of different control bandwidths in the design process. S denotes the apparent power.

The qualitative behavior again remains unchanged, and the observed trend that increased bandwidth yields better damping is confirmed. However, the change is more significant. Moreover, the bandwidth significantly influences the settling time of PI-based voltage control in the dq-frame.

In summary, we conclude for the influence of the chosen bandwidth: For the virtual admittance control design, only the current control loop is influenced, and therefore, the bandwidth influence on the considered voltage disturbance is minor. For the dq-frame PI-based voltage control architecture, the influence is significant. This can be explained by the fact that for the dq-frame implementation, the bandwidth is the only design parameter and both control loops are affected. For the PR-based voltage-control implementation in $\alpha\beta$, the bandwidth is not the only design parameter, since the peak shape is defined by additional parameters that are kept constant in this consideration; therefore, the effect of the bandwidth is less pronounced.

2) Impact of grid strength

To assess the influence of grid strength on the obtained results, we vary the SCR between 2 and 20. We again use the small-signal model to derive the closed-system eigenvalues; see Appendix A for details.

In Fig. 32 we see that the dominant damping is influenced by SCR; however, the relative rank between the different voltage control architectures is preserved.

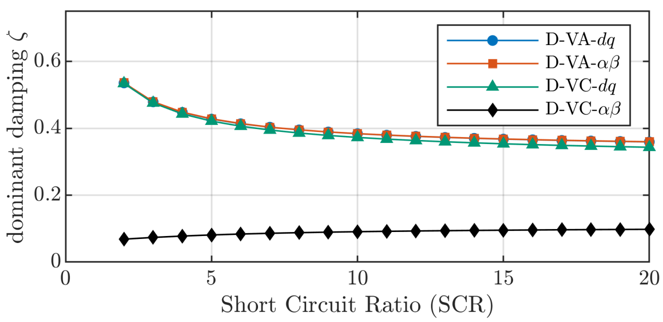

FIGURE 32. **Dominant damping over SCR range from 2-20 for parameters of Setup-A.**

Notably, the difference is smaller at small SCRs than at larger SCR values for D-VA-$\alpha\beta$, D-VA-dq and D-VC-dq. Further, for VC-$\alpha\beta$, the dominant damping is influenced the least, but slightly decreases for small SCRs and increases for larger SCRs, whereas for the D-VA-$\alpha\beta$, D-VA-dq and D-VC-dq the damping deteriorates with rising SCRs, and the variability of the dominant damping is larger over the considered SCR range.

Fig. 33 shows that the eigenvalues are affected by varying the system SCR, but the trace do to show abrupt changes regarding their relative position. This indicates that the absolute metrics are affected by SCR, but the relative comparisons can remain valid within the scope of this study.

This is further supported by exemplary time-domain results. Fig. 34 shows the voltage sag disturbance E1 for D-VA-$\alpha\beta$-t1 at the baseline SCR of 13 and a weak-grid SCR of 2.6, naturally yielding different time-domain responses. Comparing VSM-VA-$\alpha\beta$ at SCR 2.6 also shows that the influence of primary control for E1 is small, and a similar apparent-power response is obtained. The same qualitative result is obtained for the corresponding PR-based voltage control architecture as depicted in Fig. 35.

By comparing Fig. 34 and Fig. 35, the results obtained by tracing the eigenvalues of the small-signal model for different SCRs are supported as the behavior in terms of absolute power changes, but the qualitative differences between the control architectures, e.g., with respect to damping and initial overshoot, are preserved over the considered SCR range.

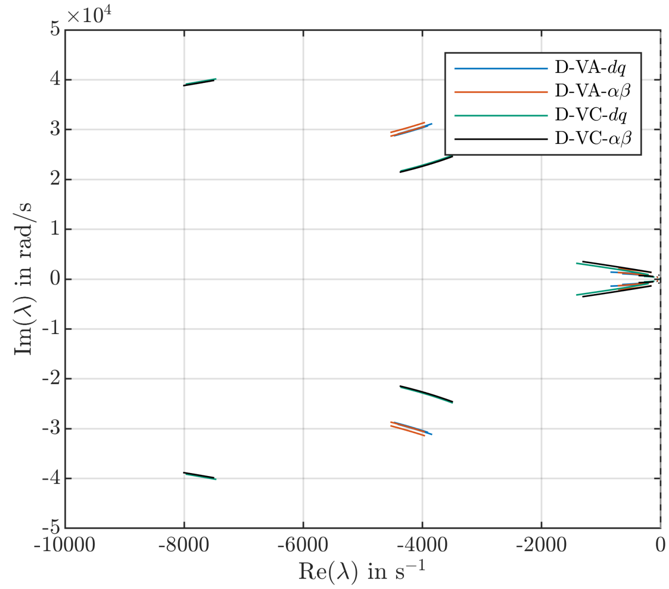

FIGURE 33. **Eigenvalue traces over a SCR range from 2-20 for the parameters of Setup-A, assuming uniform scaling of the equivalent grid impedance with SCR.**

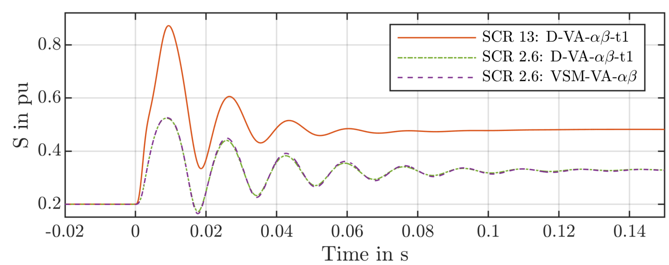

FIGURE 34. **Comparison of D-VA-$\alpha\beta$-t1 at the baseline SCR of 13 with D-VA-$\alpha\beta$-t1 and VSM-VA-$\alpha\beta$ at SCR 2.6 for results for Setup-A scenario E1.**

3) Impact of inertia in primary control tuning

To evaluate the tuning influence for the VSM-based primary control scheme, a tuning variant with doubled inertia (VSM-VA-$\alpha\beta$-h, see Table 3) is considered. The results of doubled inertia for E3 are shown in Fig. 36 for Setup-A and Fig. 37 for Setup-B.

With respect to the performance metrics, we observe the following:

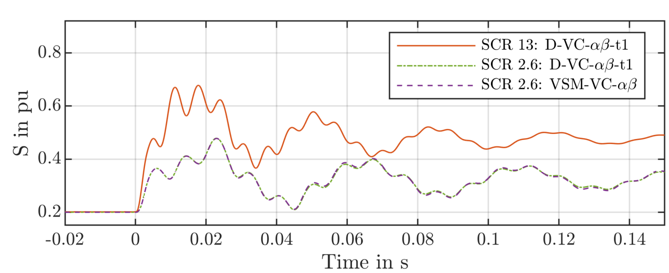

FIGURE 35. **Comparison of D-VC-$\alpha\beta$-t1 at the baseline SCR of 13 with D-VC-$\alpha\beta$-t1 and VSM-VC-$\alpha\beta$ at SCR 2.6 for results for Setup-A scenario E1.**

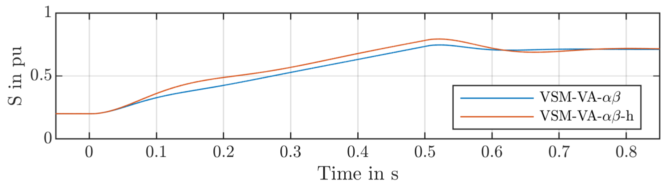

FIGURE 36. **Comparison of VSM-VA-$\alpha\beta$ with $H = 0.5$ and VSM-VA-$\alpha\beta$-h with $H = 1$ for scenario E3 and Setup-A showing the influence of increased inertia. S denotes the apparent power.**

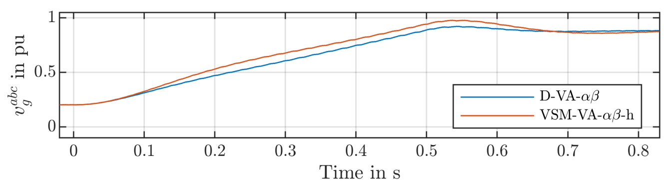

FIGURE 37. **Comparison of VSM-VA-$\alpha\beta$ with $H = 0.5$ and VSM-VA-$\alpha\beta$-h with $H = 1$ for scenario E3 and Setup-B showing the influence of increased inertia. S denotes the apparent power. Note that the differences in steady-state values compared to the simulation results stem from the different base frequencies.**

- *Settling time* T_{set}: For the angle related scenarios E2 and E3, the settlings times increase with the inertia. As expected, the voltage-related scenario E1 is not affected in the same manner.
- *Active power injection* P_{int}: The injected active power is larger for the angle-related scenarios E2 and E3 for the tuning with increased inertia. This is in accordance with expectation.

In summary, the tuning of the inertia influences the settling time T_{set} as well as the injected power P_{int}. The other transient properties, such as maximum current $I_{\max}$, oscillation index N_{osc}, or the voltage-related measures, are not influenced significantly. The influence of the primary control is relatively small when evaluating grid-support performance metrics for voltage support in the step-change scenarios E1 and E2, compared with other influences. The inertia value predominantly influences the injected active power during E3, as expected.

4) Impact of peak shape for resonant control tuning

As discussed in the current control design in Section II.B and in the context of the influence of the chosen control bandwidth in Section III.G.1 the shape of the resonant peak can be tuned independently of the bandwidth of the current control loop using $p_{g,cc}$ and ω_c for the PR $\alpha\beta$-frame implementation. This yields vastly different responses that are not apparent when bandwidth is used as a tuning metric. In the following, we analyze the influence of the resonant peak shape of the stationary reference frame realization. For comparison, we consider two tuning variants with smaller gain values for the resonant peak, but the same gain crossover frequency: D-VA-$\alpha\beta$-t2 and D-VA-$\alpha\beta$-t3, see Table 3. For the considered performance metrics, we obtain the following:

- *Voltage support* V_{rms}^{10c}: The results show that the less-aggressive current controller tuning, D-VA-$\alpha\beta$-t2 and D-VA-$\alpha\beta$-t3, increases the voltage support during voltage sag scenario E1 for both setups. The values for V_{rms}^{10c} are improved, due to a more pronounced power injection (see Fig. 38 for Setup-A). Note that for E2 and E3, the increased reactive power causes slightly impaired values for V_{rms}^{10c}.
- *Voltage nadir* $V_{\mathrm{p,min}}^{5c}$: Again, the less aggressive current controller tuning, D-VA-$\alpha\beta$-t2 and D-VA-$\alpha\beta$-t3, improves $V_{\mathrm{p,min}}^{5c}$. Especially the initial voltage undershoot in E1 is mitigated, which is a significant advantage. Again, for E2 and E3, slightly impaired values for $V_{\mathrm{p,min}}^{5c}$ are observed.
- *Settling time* T_{set}: The more sustained reaction of the less aggressively tuned current controllers is also reflected in longer settling times T_{set} for E1 and E3 for both setups. For scenario E2 in Setup-B, the settling times are shorter due to a less pronounced overshoot resulting from the less aggressive tuning.
- *Maximum current* $I_{\max}$: In accordance with the slower response observed for D-VA-$\alpha\beta$-t2 and D-VA-$\alpha\beta$-t3, the values of the maximum current $I_{\max}$ are increased significantly for several experiments, e.g. E1 and E2 Setup-A (see Table 4 and Table 6) and Setup-B E3 see Table 9.
- *Active power injection* P_{int}: For E1 and E2, the tuning variants D-VA-$\alpha\beta$-t2 and D-VA-$\alpha\beta$-t3 yield improved active power injection values to facilitate resynchronization, which is desired behavior according to emerging GFM standards [7].

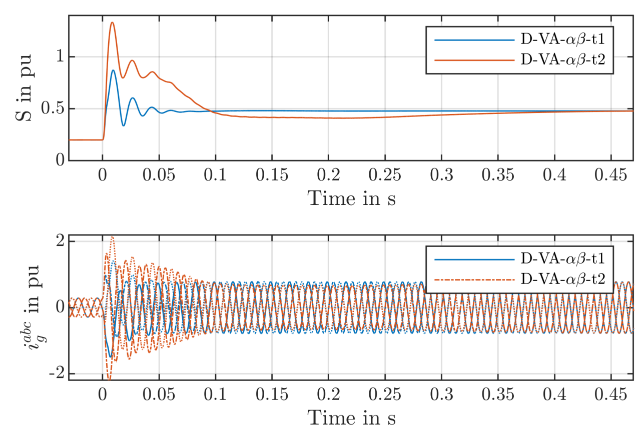

FIGURE 38. **Comparison D-VA-$\alpha\beta$-t1 and D-VA-$\alpha\beta$-t2 E1 Setup-A, showing the influence of different tuning of the current control in $\alpha\beta$-frame. The different line styles represent the phases. S denotes the apparent power.**

The counter-intuitive behavior that the less aggressive tuning of the current controller for D-VA-$\alpha\beta$-t2/3 yields improved response in terms of voltage support can be explained as follows.

Considering the injected grid current:

$$\frac{\mathrm{d}i_g^{\alpha\beta}}{\mathrm{d}t} = \frac{1}{L_i}\left(-R_i i_g^{\alpha\beta} + v_{\mathrm{mod}}^{\alpha\beta} - v_g^{\alpha\beta}\right), \tag{40}$$

where the driving force for the grid current $i_g^{\alpha\beta}$ is the difference between the modulation voltage $v_{\mathrm{mod}}^{\alpha\beta}$ and the grid voltage $v_g^{\alpha\beta}$. During the voltage sag scenario E1, the magnitude of $v_g^{\alpha\beta}$ drops and yields an increase in the grid current, assuming that the modulation voltage $v_{\mathrm{mod}}^{\alpha\beta}$ remains initially unchanged. This would be the reaction of a stiff voltage source. The desired behavior of a GFM inverter is that of a voltage source with droop behavior, which allows both the natural injection of current in response to grid disturbances [7] and parallel operation of multiple GFM inverters.

Since $v_{\mathrm{mod}}^{\alpha\beta}$ is the output of the current control loop, we now examine its behavior: in the initial time following the voltage sag, the magnitudes of the current control inputs $i_{\mathrm{ref}}^{\alpha\beta}$ and $v_{\mathrm{ff}}^{\alpha\beta}$ can be assumed constant due to low-pass behavior. For $i_{\mathrm{ref}}^{\alpha\beta}$, this is due to the virtual admittance, and for the magnitude of $v_{\mathrm{ff}}^{\alpha\beta}$, due to the low-pass filtered measurement, see (23). The modulation voltage is then reduced, driven by the current controller dynamics based on the resulting deviation $i_{\mathrm{ref}}^{\alpha\beta} - i_g^{\alpha\beta}$, see Fig. 6. Therefore, a smaller peak gain of the controller yields a slower transition to the new steady-state value and better preserves the naturally injected current, see Fig. 38.

Current control loops for IBRs are typically tuned to quickly track the reference current from the outer control loops, using large gains. This is reasonable for nominal operation, where the fast rejection of disturbances is desirable to follow the given current reference. However, during grid disturbances, a rapid increase or decrease in naturally injected current due to changes in the grid state may not be beneficial from a grid-support perspective. This constitutes a trade-off between a sufficiently large gain to follow the current reference and a reduced gain that supports the natural voltage-source behavior. Considering the time domain results for Setup-A with D-VA-$\alpha\beta$-t2 in Fig. 38 and Setup-B with D-VA-$\alpha\beta$-t3 in Fig. 39, also shows that smaller gains yield significantly slower convergence to the new steady state.

Considering this trade-off, the current control tuning for PR-based controllers is a viable option for shaping the initial response of IBRs to grid disturbances.

IV. Design-Oriented Discussion of the Results

This section summarizes the design implications of the obtained results. Naturally, the conclusions are limited to the investigated setups, disturbance scenarios as well as the deployed tuning procedures detailed in Sec. II. Further, the disturbance scenarios are designed not to trigger current limitations and only consider balanced disturbances.

For a concise overview of controller properties and selection guidelines, Table 11 summarizes the simplified key

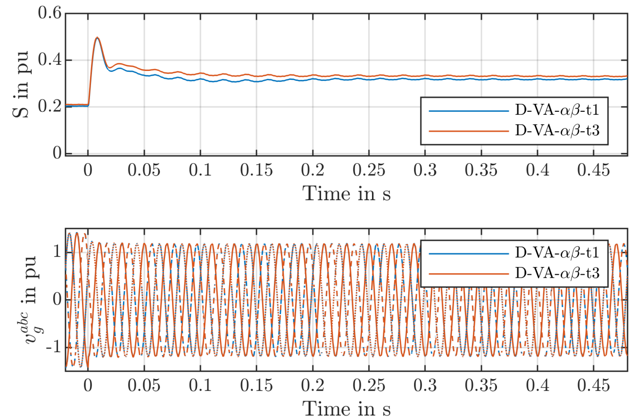

FIGURE 39. Comparison D-VA-$\alpha\beta$-t1 and D-VA-$\alpha\beta$-t3 for Setup-B scenario E1, showing the influence of different tuning of the current control in $\alpha\beta$-frame. Note that the steady state is altered for small peak gains. The different line styles represent the phases. S denotes the apparent power.

characteristics of each architecture. The following design-oriented discussion expands on these insights:

- *Voltage control architecture:* For $\alpha\beta$-frame implementations, virtual-admittance control provides superior damping compared to PR-based voltage control. For dq-frame implementations, oscillatory performance differs little between virtual-admittance control and PI-based voltage control. For both reference frames, the virtual-admittance-based control yields larger maximum currents for E1 and E2, see Tables 4 – 7. This creates a trade-off between risking current limitation and providing fault current.
- *Choice of reference frame:* For virtual-admittance control, the choice of reference frame leads to only minor differences in disturbance response. However, when closed-loop voltage control is required, the dq-frame PI implementation provides notably better damping than the $\alpha\beta$-frame PR-based counterpart.
  A key distinction lies in tuning flexibility: the dq-frame PI controllers rely solely on bandwidth as a design parameter, making the disturbance response highly sensitive to bandwidth selection—particularly for cascaded voltage control where both loops are affected. In contrast, $\alpha\beta$-frame PR controllers offer additional degrees of freedom through resonant peak shaping parameters ($p_{g,cc}$, ω_c), enabling response shaping independent of bandwidth, as shown in Sec. III.G.4.
  This structural difference introduces an inherent limitation: although we aim to match gain crossover frequencies and verify similar open-loop characteristics, the observed performance differences cannot be attributed with full certainty to architecture alone. That said, the consistent behavior across tuning variations, both test setups, and supporting small-signal analysis suggests the effects are not purely tuning artifacts. Nevertheless, absolute performance rankings may shift under alternative tuning strategies.

TABLE 11. Summary of design-oriented insights for the compared control architectures. Note that this summary presents tendencies observed and might not hold for all setups and disturbance scenarios; for a detailed discussion, please refer to Sec. III.

Architecture	Tuning Parameters	Damping	$I_{\max}$	Advantages	Disadvantages
VA-$\alpha\beta$	5	High	Highest	Best damping, tuning flexibility via resonance peak shaping, good initial support with high $I_{\max}$	High $I_{\max}$ increases momentary overcurrent risk during step disturbances, requiring hardware margin, no inherent frequency tracking, no closed-loop voltage regulation
VA-dq	4	High	High	Best damping, good initial support with high $I_{\max}$	High $I_{\max}$ increases momentary overcurrent risk during step disturbances, requiring hardware margin, no closed-loop voltage regulation
VC-$\alpha\beta$	6	Low	Low	Low $I_{\max}$ reduces overcurrent risk, closed-loop voltage regulation, tuning flexibility via resonant peak shaping	Poor damping for step disturbances, sometimes sluggish settling times, no inherent frequency tracking
VC-dq	4	Mod.–High	Low	Good damping, low $I_{\max}$ reduces overcurrent risk, closed-loop voltage regulation	High bandwidth sensitivity
Primary Control Options					
Droop	3 (additional)	—	—	Simple implementation and interpretation, widely deployed	No dedicated parameters for inertia or damping emulation (dependent on droop and filter gains), limited transient shaping capability
VSM	5 (additional)	—	—	Inertia emulation, independently tunable damping	More complex tuning

- *Primary control:* In the investigated cases, both primary control approaches have the same reactive-power-voltage droop but differ in their angle dynamics. Consequently, only a minor influence is observed in the voltage disturbance E1 case for both setups, see Tables 4 and 5.
  By contrast, the angle-related scenarios E2 and E3 show a different impact. In these scenarios, the VSM-based approach can tune damping, inertia, and steady-state behavior individually, offering more degrees of freedom in shaping the response. For E3, the effect of the primary control is weaker in the time-domain response, although differences remain visible in the settling-time metric.
  Overall, the influence of primary control for the fast timescale focus in this study is smaller than that of other control architecture choices. More generally, the impact of the primary control depends on the interactions among angle dynamics, voltage dynamics, and power flow, which, in turn, are strongly influenced by the grid strength as discussed in Sec. III.G.2.
- *Current control tuning:* The current control loop provides an additional degree of freedom for shaping the fast-timescale disturbance response, particularly for $\alpha\beta$-frame PR implementations. Disturbance behavior is influenced less by the chosen bandwidth than by the resonant peak shape: smaller peak gains ($p_{g,cc}$) improve grid support metrics by better preserving the naturally injected current during grid incidents, at the cost of slower reference tracking. This trade-off should be considered when selecting current control parameters, as aggressive tuning prioritizes reference tracking while reduced gains enhance fault-current contribution. For dq-frame PI current control, bandwidth is the sole design parameter, yielding higher sensitivity to bandwidth variations but simpler tuning.

V. Conclusion

The present paper systematically analyzes how control architectures and parameter tuning, particularly of the inner control loops, shape the transient response of grid-forming inverters to grid disturbances. The study is conducted within a consistent design and comparison framework combining simulation and hardware-based experiments using two complementary single-inverter infinite-bus systems with distinct parameters. The considered scenarios cover balanced grid disturbances without current-limiter activation.

The results show that inner-loop architecture and tuning significantly affect the fast-timescale disturbance response. For the considered systems and tuning procedures, the reference frame, the voltage control architecture, and the peak shape design for resonant current controllers are found to strongly influence damping, oscillatory behavior, and peak current values on a fast timescale. These findings highlight that common design assumptions in inner-loop design can significantly affect converter behavior during disturbances.

Within the scope of the investigated setups and deployed tuning procedures, the study provides design-oriented insights for practical controller selection and tuning. Future work should extend the analysis to unbalanced fault conditions, as they are a critical aspect of real power grids. More broadly, the results underline the need for transparent reporting of inner control implementations and tuning procedures to improve clarity and reproducibility in inverter-based resource control research.

REFERENCES

[1] Y. Gu and T. C. Green, "Power System Stability With a High Penetration of Inverter-Based Resources," *Proceedings of the IEEE*, vol. 111, no. 7, pp. 832–853, Jun. 2023.
[2] J. Wachter, L. Gröll, and V. Hagenmeyer, "Survey of Real-World Grid Incidents–Opportunities, Arising Challenges and Lessons Learned for the Future Converter Dominated Power System," *IEEE Open Journal of Power Electronics*, vol. 5, pp. 50–69, Dec. 2023.
[3] B.-M. S. Hodge, H. Jain, C. Brancucci, G.-S. Seo, M. Korpås, J. Kiviluoma, H. Holttinen, J. C. Smith, A. Orths, A. Estanqueiro *et al.*,

"Addressing technical challenges in 100% variable inverter-based renewable energy power systems," *Wiley Interdisciplinary Reviews: Energy and Environment*, vol. 9, no. 5, pp. 1–19, May 2020.

[4] A. Hoke, M. Rasel, A. Nelson, D. Pattabiraman, M. Asano, D. Arakawa, B. Pierre, M. Elkhatib, J. Tan, V. Gevorgian, C. Antonio, and E. Ifuku, "Fast Grid Frequency Support from Distributed Energy Resources," Grid Modernization Laboratory Consortium US Departement of Energy, Tech. Rep., 2021. [Online]. Available: https://www.nrel.gov/docs/fy21osti/71156.pdf

[5] Y. Lavi and J. Apt, "Inverter fast frequency response is a low-cost alternative to system inertia," *Electric Power Systems Research*, vol. 221, pp. 1–10, Aug. 2023.

[6] VDE, "Power Generating Plants in the Low Voltage Network (VDE-AR-N 4105)," VDE, Tech. Rep. VDE-AR-N 4105, 2018.

[7] B. Kroposki, "Unifi specifications for grid-forming inverter-based resources: Version 3," National Laboratory of the Rockies (NLR), Golden, CO (United States), Tech. Rep., 2026.

[8] M. S. Misaghian, C. O'Dwyer, and D. Flynn, "Fast frequency response provision from commercial demand response, from scheduling to stability in power systems," *IET Renewable Power Generation*, vol. 16, no. 9, pp. 1908–1924, Jul. 2022.

[9] G.-S. Seo, M. Colombino, I. Subotic, B. Johnson, D. Groß, and F. Dörfler, "Dispatchable virtual oscillator control for decentralized inverter-dominated power systems: Analysis and experiments," in *Proc. 2019 IEEE Applied Power Electronics Conference and Exposition (APEC)*, 2019, pp. 561–566.

[10] P. Unruh, M. Nuschke, P. Strauß, and F. Welck, "Overview on Grid-Forming Inverter Control Methods," *Energies*, vol. 13, no. 10, pp. 1–21, May 2020.

[11] C. Schöll and H. Lens, "Design- and simulation-based comparison of grid-forming converter control concepts," in *Proceedings of 20th International Workshop on Large-Scale Integration of Wind Power into Power Systems as Well as on Transmission Networks for Offshore Wind Power Plants (WIW 2021)*, Germany, 2021, pp. 310–316.

[12] D. B. Rathnayake, M. Akrami, C. Phurailatpam, S. P. Me, S. Hadavi, G. Jayasinghe, S. Zabihi, and B. Bahrani, "Grid Forming Inverter Modeling, Control, and Applications," *IEEE Access*, vol. 9, pp. 1–27, Aug. 2021.

[13] A. J. Abrantes-Ferreira and A. M. Lima, "Comparative Performance Analysis of Grid-Forming Strategies Applied to Disconnectable Microgrids," in *Proceedings of Brazilian Power Electronics Conference (COBEP)*, Nov. 2021, pp. 01–08.

[14] Z. Jin and X. Wang, "A DQ -Frame Asymmetrical Virtual Impedance Control for Enhancing Transient Stability of Grid-Forming Inverters," *IEEE Transactions on Power Electronics*, vol. 37, no. 4, pp. 4535–4544, Nov. 2022.

[15] M. Gursoy and B. Mirafzal, "Direct vs. Indirect Control Schemes for Grid-Forming Inverters–Unveiling a Performance Comparison in a Microgrid," *IEEE Access*, vol. 11, pp. 1–14, Jul. 2023.

[16] A. Narula, M. Bongiorno, and M. Beza, "Comparison of Grid-Forming Converter Control Strategies," in *Proceedings of IEEE Energy Conversion Congress and Exposition (ECCE)*, 2021, pp. 361–368.

[17] A. Oshnoei and F. Blaabjerg, "Sliding Mode-based Model Predictive Control of Grid-Forming Power Converters," in *Proceedings of European Control Conference (ECC)*, 2023, pp. 1–6.

[18] M. Beza and M. Bongiorno, "Impact of converter control strategy on low- and high-frequency resonance interactions in power-electronic dominated systems," *International Journal of Electrical Power & Energy Systems*, vol. 120, pp. 1–15, Sep. 2020.

[19] B. Yang, N. Baeckeland, and G.-S. Seo, "Small-signal analysis of current-limiting grid-forming inverters," *IEEE Trans. Ind. Appl.*, accepted.

[20] P. Rodriguez, I. Candela, and A. Luna, "Control of PV generation systems using the synchronous power controller," in *Proceedings of IEEE Energy Conversion Congress and Exposition*, 2013, pp. 993–998.

[21] J. D. V. Leon, A. Tarraso, J. I. Candela, J. Rocabert, and P. Rodriguez, "Grid-Forming Controller Based on Virtual Admittance for Power Converters Working in Weak Grids," *IEEE Journal of Emerging and Selected Topics in Industrial Electronics*, vol. 4, no. 3, pp. 791–801, Jul. 2023.

[22] L. Zhao, X. Wang, H. Gong, and Z. Jin, "Stability Impact of Hybrid Synchronization Strategy on Virtual-Admittance-Based Grid-Forming Inverters," in *Proceedings of IEEE Applied Power Electronics Conference and Exposition (APEC)*, 2023, pp. 2735–2740.

[23] X. Wang, Y. W. Li, F. Blaabjerg, and P. C. Loh, "Virtual-Impedance-Based Control for Voltage-Source and Current-Source Converters," *IEEE Transactions on Power Electronics*, vol. 30, no. 12, pp. 7019–7037, Dec. 2015.

[24] A. Yazdani and R. Iravani, *Voltage-Sourced Converters in Power Systems: Modeling, Control, and Applications*. Hoboken, New Jersey: IEEE Press/John Wiley, 2010.

[25] N. Baeckeland, D. Venkatramanan, M. Kleemann, and S. Dhople, "Stationary-Frame Grid-Forming Inverter Control Architectures for Unbalanced Fault-Current Limiting," *IEEE Transactions on Energy Conversion*, vol. 37, no. 4, pp. 2813–2825, Dec. 2022.

[26] D. Zmood and D. Holmes, "Stationary frame current regulation of PWM inverters with zero steady-state error," *IEEE Transactions on Power Electronics*, vol. 18, no. 3, pp. 814–822, May 2003.

[27] N. Baeckeland, "Design and Modeling of Inverter Control for Fault Behavior and Power System Protection Analysis," Ph.D. dissertation, KU Leuven, 2022.

[28] J. Rocabert, A. Luna, F. Blaabjerg, and P. Rodríguez, "Control of Power Converters in AC Microgrids," *IEEE Transactions on Power Electronics*, vol. 27, no. 11, pp. 4734–4749, May 2012.

[29] J. Wachter, L. Gröll, and V. Hagenmeyer, "Application of Model-Free Control to Reduce the Total Harmonic Distortion of Inverters," in *Proceedings of 8th IEEE Workshop on the Electronic Grid (eGRID)*, 2023, pp. 1–7.

[30] K. J. Åström and T. Hägglund, *Advanced PID Control*. North Carolina, USA: ISA, 2006.

[31] P. Rodriguez, I. Candela, C. Citro, J. Rocabert, and A. Luna, "Control of grid-connected power converters based on a virtual admittance control loop," in *Proceedings of IEEE 5th European Conference on Power Electronics and Applications (EPE)*, 2013, pp. 1–6.

[32] W. Zhang, A. M. Cantarellas, J. Rocabert, A. Luna, and P. Rodriguez, "Synchronous Power Controller With Flexible Droop Characteristics for Renewable Power Generation Systems," *IEEE Transactions on Sustainable Energy*, vol. 7, no. 4, pp. 1572–1582, Oct. 2016.

[33] W. Zhang, A. Tarraso, J. Rocabert, A. Luna, J. I. Candela, and P. Rodriguez, "Frequency Support Properties of the Synchronous Power Control for Grid-Connected Converters," *IEEE Transactions on Industry Applications*, vol. 55, no. 5, pp. 5178–5189, Sep. 2019.

[34] N. Baeckeland, D. Chatterjee, M. Lu, B. Johnson, and G.-S. Seo, "Overcurrent limiting in grid-forming inverters: A comprehensive review and discussion," *IEEE Trans. Power Electron.*, vol. 39, no. 11, pp. 14 493–14 517, Nov. 2024.

[35] IEEE, "IEEE Application Guide for IEEE Std 1547™-2018, IEEE Standard for Interconnection and Interoperability of Distributed Energy Resources with Associated Electric Power Systems Interfaces."

[36] NERC Inverter-Based Resource Performance Task Force (IRPTF), "Fast Frequency Response Concepts and Bulk Power System Reliability Needs," NERC, Tech. Rep., 2020. [Online]. Available: https://www.nerc.com/comm/PC/InverterBased%20Resource%20Performance%20Task%20Force%20IRPT/Fast_Frequency_Response_Concepts_and_BPS_Reliability_Needs_White_Paper.pdf

[37] Hawaii Grid, "RULE NO. 30 MICROGRID SERVICES," HAWAII ELECTRIC LIGHT COMPANY, INC., Tech. Rep., 2021. [Online]. Available: https://www.hawaiianelectric.com/documents/billing_and_payment/rates/hawaii_electric_light_rules/30.pdf

[38] R. Teodorescu, M. Liserre, and P. Rodríguez, *Grid Converters for Photovoltaic and Wind Power Systems*. Chichester, United Kingdom: Wiley, 2011.

[39] P. Rodriguez, J. Pou, J. Bergas, J. I. Candela, R. P. Burgos, and D. Boroyevich, "Decoupled Double Synchronous Reference Frame PLL for Power Converters Control," *IEEE Transactions on Power Electronics*, vol. 22, no. 2, pp. 584–592, Mar. 2007.

[40] M. Reyes, P. Rodriguez, S. Vazquez, A. Luna, J. M. Carrasco, and R. Teodorescu, "Decoupled Double Synchronous Reference Frame current controller for unbalanced grid voltage conditions," in *Proceedings of IEEE Energy Conversion Congress and Exposition (ECCE)*, 2012, pp. 4676–4682.

[41] N. Baeckeland, B. Yang, and G.-S. Seo, "Transient Stability-Enhancing Method for Grid-Forming Inverters Under Current Limiting," *IEEE Transactions on Power Electronics*, vol. 40, no. 5, pp. 6714–6725, Jan. 2025.

[42] *TPI 8032 22kW - all-in-one programmable inverter*, Imperix, datasheet. [Online]. Available: https://imperix.com/wp-content/uploads/document/TPI8032_Datasheet.pdf

[43] F. Wiegel, J. Wachter, M. Kyesswa, R. Mikut, S. Waczowicz, and V. Hagenmeyer, "Smart Energy System Control Laboratory – a fully-automated and user-oriented research infrastructure for controlling and operating smart energy systems," *at - Automatisierungstechnik*, vol. 70, no. 12, pp. 1116–1133, Dec. 2022.

Appendix

A. Small-signal model and comparison metrics

To compare the dynamic behavior of the different control architectures, a small-signal model is used as derived in the following.

1) State-space formulation

The closed-loop system of the single inverter infinite-bus setup, see Fig.1, is represented in converter-synchronous coordinates as a state-space model:

$$\dot{x} = f(x, p)\,, \tag{41}$$

where $x \in \mathbb{R}^{n_x}$ denotes the state vector and p contains physical and controller parameters. The specific structure of $f(\cdot)$ and the dimension n_x depend on the chosen control architecture (reference frame, voltage control type and primary control).

For $\alpha\beta$-frame implementations with PR controllers, the stationary-frame controller states are transformed into synchronous coordinates via $z_{dq} = T(\theta) z_{\alpha\beta}$.

2) Equilibrium and Linearization

The operating point x_{eq} is obtained by solving $f(x_{eq}) = 0$ using numerical methods. Small-signal linearization yields:

$$\Delta\dot{x} = A\Delta x, \quad A = \left.\frac{\partial f}{\partial x}\right|_{x=x_{eq}}, \tag{42}$$

where $A \in \mathbb{R}^{n_x \times n_x}$ is the state matrix computed via numerical Jacobian linearization. From this, the following metrics are derived:

- *Stability:* Determined by the rightmost closed-loop pole location in the complex plane. The system is stable when all eigenvalues satisfy $\mathrm{Re}(\lambda_k) < -\delta$, where $\delta = 10^{-6}$ is used as the stability tolerance and $k = 1 \dots n_x$.
- *Dominant damping ratio:* is defined as the damping ratio of the stable eigenvalue with maximum real part λ_d and calculated as following
$$\zeta = \frac{-\mathrm{Re}(\lambda_d)}{|\lambda_d|}\,. \tag{43}$$
- *Number of excited oscillatory modes:* are counted as stable complex-conjugate pole pairs satisfying $|\mathrm{Im}(\lambda_i)| > \omega_{\text{th}}$ and $\eta_i > \gamma \cdot \max_j(\eta_j)$, where λ_i denotes the i-th eigenvalue, $\eta_i = |l_i^\top B_d| \cdot \|r_i\|$ is the modal excitation metric, r_i and l_i are the corresponding right and left eigenvectors, B_d is the disturbance input matrix, $\omega_{\text{th}} = 10\,\text{rad/s}$ is the oscillation threshold, and $\gamma = 0.08$ is the excitation significance threshold. The disturbance input matrices B_d are obtained via $B_d = \frac{\partial \dot{x}}{\partial d}\big|_{x=x_{eq},\, d=d_0}$, where d denotes the considered disturbance and d_0 the equilibrium value of the disturbance.
- *Disturbance damping quality:* denoted by ζ_{osc} is calculated as an excitation-weighted average of damping ratios for significantly excited stable modes. For each disturbance (voltage sag or angle jump), the significant mode set $\mathcal{S}_d = \{i : \mathrm{Re}(\lambda_i) < 0 \text{ and } \eta_i > \gamma \cdot \max_j(\eta_j)\}$ is identified using the same modal excitation metric η_i and threshold $\gamma = 0.08$ as above. The weighting factors are $w_i = \eta_i^p / \sum_{k\in\mathcal{S}_d} \eta_k^p$ with exponent $p = 2$ (squared weighting), and the final metric is $\zeta_{osc} = \sum_{i\in\mathcal{S}_d} w_i \cdot \zeta_i$, where $\zeta_i = -\mathrm{Re}(\lambda_i)/|\lambda_i|$ is the damping ratio of the i-th mode. Higher values indicate better overall damping of excited modes.